Countercurrent Imbibition in Porous Media with Dense and Parallel Micro-Fractures: Numerical and Analytical Study

Fei Yu[1,2]#, Rujun Han[1]#, and Ke Xu[1]*

[1]Department of Energy and Resource Engineering, College of Engineering, Peking University, Beijing, China
[2]Sinopec Research Institute of Petroleum Engineering, Beijing, China

*Corresponding author; email: kexu1989@pku.edu.cn

Summary

Countercurrent imbibition is the process in which the wetting fluid spontaneously displaces the non-wetting fluid, while the non-wetting fluid is recovered at the wetting fluid inlet. It is a major mechanism for the recovery of shale oil, shale gas and tight oil. In shale and tight formations, micro-fractures are highly developed. Specifically, some typical formations, such as continental shales, consist of dense and parallel micro-fractures (DPF). In DPF systems, micro-fractures are segregated by low-permeability matrix, that breaks underlying assumptions of classical dual-porosity (DP) model. However, very close distance between neighboring micro-fractures results in strong capillary correlation. Despite extensive studies on layered media, there is still no suitable model to describe imbibition in DPF system at the representative elementary volume (REV) scale.

In this study, we first numerically simulate the countercurrent imbibition in DPF systems with fine grids, adopting typical continental shale parameters. For imbibition parallel to micro-fractures, two distinct stages are identified: an early stage where fractures are not correlated, and a late stage where neighboring fractures are strongly correlated by capillarity. In both stages, cumulative oil production (Q) is proportional to the square root of imbibition time ($t^{1/2}$), while the pre-factors are very different. The late stage is the dominant stage in oil recovery. We note that the matrix permeability rarely contributes to imbibition parallel to micro-fractures at the late time, indicating that the matrix's role here is to store fluid rather than to provide flow resistance. In addition, we rationalize the failure of classical DP model, as it significantly overestimates fracture-matrix fluid exchange near the displacement front. Similarly, for imbibition perpendicular to micro-fractures, Q is also proportional to $t^{1/2}$ in late stage.

After elucidating the mechanisms of fracture-fracture capillary interaction, we successfully derive analytical solutions for countercurrent imbibition kinetics in DPF at the late stage. We accordingly propose equivalent REV scale model and examine it with fine-grid simulations. We highlight the importance of adopting anisotropic relative permeability in this DPF system at REV scale for reservoir simulation, rather than simply adopting anisotropic absolute permeability. This presents a new challenge for numerical simulations at reservoir scale.

I. Introduction

The increasing global demand and ever-tightening supply of conventional hydrocarbons are driving significant expansion of unconventional resource production, which have huge reserves in shale and tight formations (Xu et al. 2022; Muther et al. 2022; Zou et al. 2013). Compared to conventional reservoirs, shales have lower porosity and permeability with highly developed micro-fractures (Sinn et al. 2017; Ma et al. 2019; Meng et al. 2020).

Spontaneous countercurrent imbibition is a major mechanism for unconventional hydrocarbon recovery (Gu et al. 2019) after hydraulic fracturing. During countercurrent imbibition, more wetting aqueous fluid spontaneously displaces less wetting oil/gas in the low permeability matrix driven by capillary forces, and the two phases flow in opposite directions (Schmid et al. 2016). Countercurrent imbibition has been well investigated in conventional formation. There are many studies focusing on either the evaluation of imbibition recovery (Polat 2021; Tian et al. 2021; Hatiboglu and Babadagli 2007; Q. Meng et al. 2019) or the countercurrent imbibition distance (Meng, Liu, and Wang 2016) by using experimental, theoretical and numerical approaches. For homogeneous media, it has been

experimentally and theoretically shown that the recovery evolution with time is diffusive, i.e., recovery is proportional to the square root of imbibition time (Mcwhorter and Sunada 1990; Schmid et al. 2016; Velasco-Lozano and Balhoff 2021). However, recent reports on core flood experiments in low permeability formation (Lukyanov et al. 2019; Sirimark, Lukyanov, and Pryer 2018; 2019; Lukyanov et al. 2012) show some super-diffusive imbibition kinetics at early imbibition stage, i.e., recovery evolves faster than square root of imbibition time. Although some hypotheses are proposed to rationalize these super-diffusive imbibition kinetics, there is still very few well-accepted theories for this. It is highly suspected that the microscale geometric features in these low permeability media reshapes the imbibition kinetics.

Specifically, continental shales consist of dense and parallel micro-fractures (DPF), as shown in **Fig. 1a, b, c, d** (Wang, Lyu, and Cole 2019; Sun et al. 2022). The population density of parallel micro-fractures in continental shale can be as large as 4000 /m (Panahi et al. 2013; Ougier-Simonin et al. 2016; Kobchenko et al. 2011). To model the flow in such DPF systems for reservoir simulation, discrete fracture models and embedded discrete fracture models are not computationally affordable, so elementary volume (REV) scale model is necessary. In an REV scale model, layered micro-fractures and low-permeability porous matrix should be ''averaged''. However, micro-fractures in continental shales are poorly connected, making classical dual-porosity (DP) model (Barenblatt, Zheltov, and Kochina 1960; Warren and Root 1963; Kazemi et al. 1976) not suitable due to the failure of interconnecting fracture assumption. Meanwhile, the distance of neighboring micro-fractures is so close that they could be hydrodynamically coupled by capillarity correlation through the thin matrix between them during multiphase flow. Consequently, approaches on independent single fracture (Andersen 2019; Andersen, Evje, and Kleppe 2014; Velasco-Lozano and Balhoff 2021) are also not applicable. There is still lack of research on spontaneous imbibition in DPF systems.
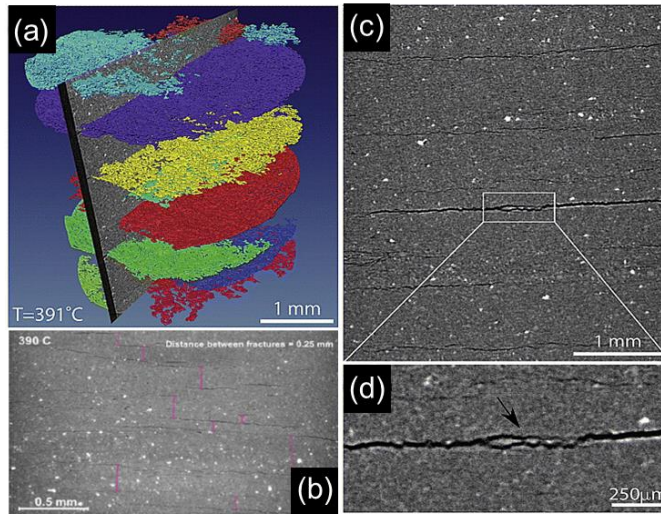
Fig. 1—Images of dense and parallel micro-fractures in shales. (a) X-ray tomography imaging of 3D micro-fracture network in shales; (b) Average distance between micro-fractures in shales; (c) Dense and parallel micro-fractures in shales; (d) Details of a single parallel micro-fracture. (a), (b), (c) and (d) are reedited from (Kobchenko et al. 2011; Ougier-Simonin et al. 2016; Panahi et al. 2013).

In this study, we aim at establishing equivalent REV scale model for multiphase flow in DPM media, referring to the realistic structure of continental shale. We first conduct fine grid numerical simulations to resolve the spatial and temporal evolution of fluid distribution during countercurrent imbibition, along or perpendicular to the micro-fractures. Based on numerical results, we can propose and validate some major assumptions and then explore theoretical correlations for imbibition along and perpendicular to micro-fractures. By contrast, we simulate using DP model and identify the reason why the DP model fails in this circumstance. According to the assumptions and theoretical correlations, we establish multiphase flow REV scale model for DPM media, and highlight the necessity of applying anisotropic relative permeability.

II. Model Development

A definition of dense and parallel micro-fracture (DPF) system.

Layered media with nearly parallel structures is geologically typical. Here, we define ''dense'' rigorously as that the characteristic time of spontaneous imbibition between fractures (t_m) is much smaller than the characteristic time of fluid flow time along fractures (t_f). Here, t_m can be estimated as $t_m = \frac{\mu_w \left(\frac{B}{2}\right)^2}{k_m p_{cm}}$ (where μ_w is the viscosity of water, B is the matrix width between micro-fractures, k_m and p_{cm} are the permeability and capillary pressure of matrix, respectively), and t_f during spontaneous imbibition can be estimated as $t_f = \frac{\mu_w (L_x)^2}{k_f p_{cf}}$ (where L_x is the length of micro-fractures, k_f and p_{cf} are the permeability and capillary pressure of micro-fractures, respectively). A

fractured media can be defined as a DPF system, only when $t_m \ll t_f$. In a typical continental shale (shown in **Fig. 1b**), $t_m \approx 10^1$ s, while $t_f = 10^4$ s, which matches the DPF system definition.

Key assumptions.

The following assumptions are made to reasonably simplify the numerical and theoretical research:

1. The porous matrix layers share identical permeability, relative permeability curves and capillary pressure curve.

2. Fluids and shale are incompressible, and two phases are immiscible.

3. The impact of gravity is negligible, which requires the Bond number $Bo = \frac{\rho_w g h}{\sigma/(b/2)} \ll 1$, where ρ_w is the density of water, g is the gravitational acceleration, h is REV thickness, σ is the water surface tension and b is the micro-fracture aperture. This assumption is valid in our cases.

4. The shale is water wet or mixed-wet, so spontaneous imbibition can occur when oil-saturated matrix is in contact with water. In the main text, we only demonstrate the results of water-wet cases. As for mixed-wet shale, we also simulate an example to validate our models and correlations in the supplementary materials (section S.I and **Fig. S-1**&**S-2**&**S-3**).

5. The flow along micro-fractures follows Darcy's law. This assumption is valid for shale gas recovery, as: 1) micro-fractures are of aperture much larger than 10^{-7} m, so nano-scale effects can be neglected; and 2) Reynolds number $Re = \frac{\rho_w u_x b}{\mu_w} \ll 1$ (Xue, Guo, and Chen 2020),where u_x is the velocity of fluid flow in x-direction in our simulation, so inertia effect is negligible. All cases discussed later satisfy $Re \ll 1$.

6. The flow in porous matrix follows Darcy's law. We note that many nonlinear flow behaviors may emerge in nanoporous media (Zhu et al. 2023; Afsharpoor and Javadpour, 2016; Cui, 2019), especially when the pore size is smaller than 10 nm. Nevertheless, movable shale oil mainly flows in relatively large pores (10 - 1000 nm) where Knudsen number (K_n) is lower than 0.1 (Roy et al. 2003; Zhang et al. 2019) , so slip-boundary effects, Knudsen diffusion and other nano-scale non-Darcy effects are not dominant (Li et al. 2019; Cui, 2019). We thus still adopt Darcy's law to attain analytical solution. Nevertheless, we are to relax this assumption later for imbibition parallel to the micro-fractures.

Model setup.

We use three different types of geometrical models, as shown in **Fig. 2a, b, c**:

1. Unidirectional imbibition parallel to the micro-fractures, denoted as x-direction model, which contains two symmetric micro-fractures, as shown in **Fig. 2a**.

2. Unidirectional imbibition perpendicular to the micro-fractures, denoted as y-direction model, which contains multiple micro-fractures, as shown in **Fig. 2b**.

3. Dual-directional imbibition in two-dimensional (2D) media, denoted by oblique imbibition model, as shown in **Fig. 2c**.

   In all geometric models, we set constant pressure boundary at the inlet, where the pressures of two phases are equal. All other boundaries are closed. The model thickness is set to be 0.5 mm. We vary the value of distance between neighboring micro-fractures (0.12 to 0.36 mm) (Ougier-Simonin et al. 2016), micro-fracture apertures (0.0025 to 0.03 mm) (Panahi et al. 2013), matrix permeabilities (0.0001 to 0.01 mD) (Meng et al. 2020), and crude oil or gas viscosities (0.01 to 100 mPa·s) (Chen et al. 2021; Wang et al. 2020), which are aligned with typical continental shale formation features and the DPF system definition.

   In addition, the fractures are parallel planes instead of parallel lines in practical three-dimension cases, with three orthogonal flow directions. As the two orthogonal directions parallel to the fracture are symmetric, we only consider the two-dimensional cases for theoretical and numerical study. Nevertheless, we still demonstrate some three-dimensional cases in supplementary material (section S.II and **Fig. S-4** & **S-5**), where we compare the fine-grid simulation, theoretical model and REV scale model.
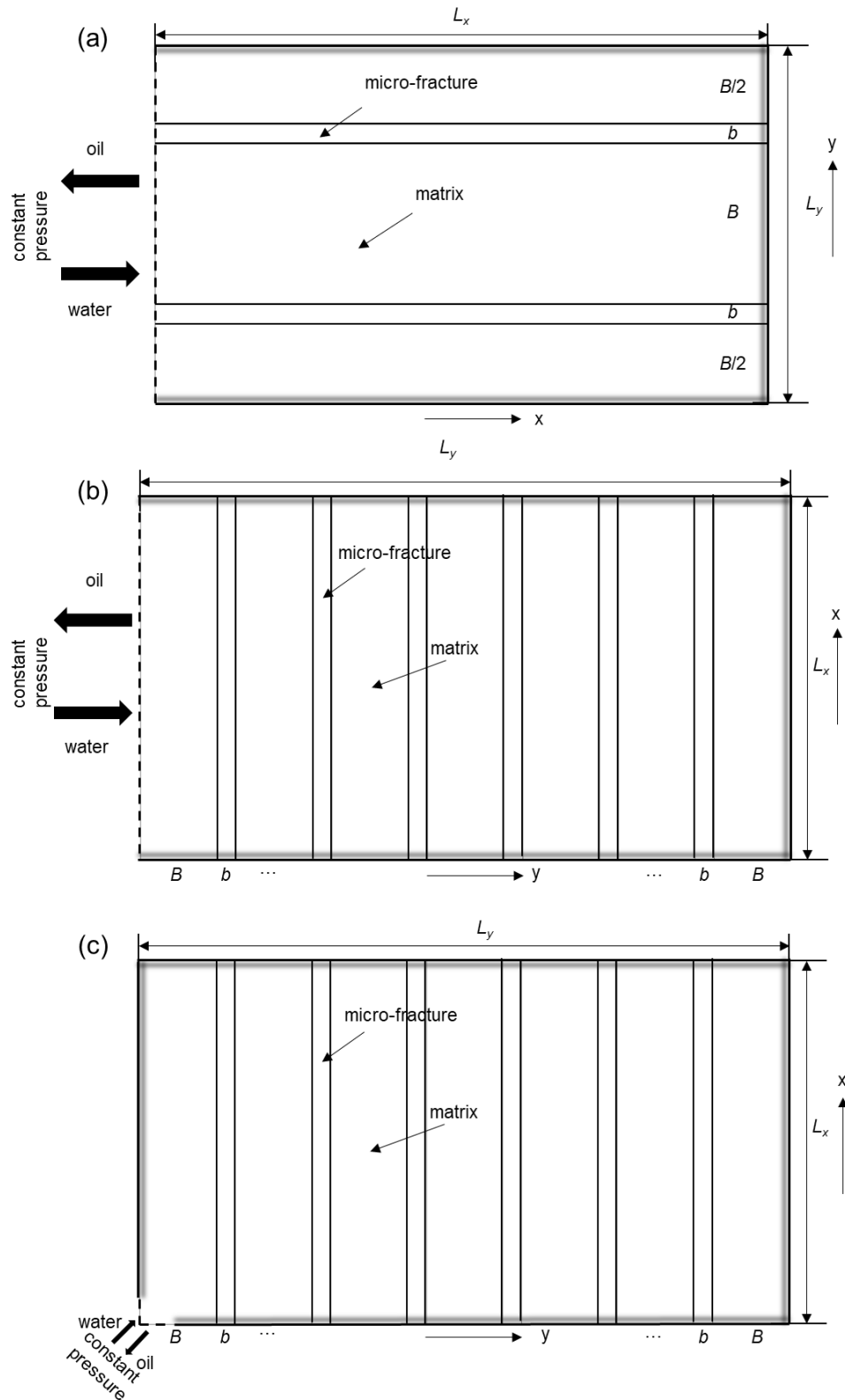
Fig. 2—Schematic simulation models of dense and parallel micro-fractures in shales. (a) x-direction model, L_x = 150 mm, L_y = 0.54 mm, b = 0.03 mm, B = 0.24 mm; (b) y-direction model, L_x = 300 mm, L_y = 32 mm, b = 0.01 mm, B = 0.24 mm; (c) Oblique imbibition model, L_x = 300 mm, L_y = 13.24 mm, b = 0.01 mm, B = 0.24 mm.

Governing equations.

The transport equations for incompressible, immiscible oil-water flow in porous rock without external source terms read:

$$\frac{\partial}{\partial t}(\phi S_o) = -\nabla \cdot (\boldsymbol{v}_o) \tag{1}$$

$$\frac{\partial}{\partial t}(\phi S_w) = -\nabla \cdot (\boldsymbol{v}_w) \tag{2}$$

where ϕ is porosity. $S_{w(o)}$ is the saturation of water(oil), and $\boldsymbol{v}_{w(o)}$ is the Darcy velocity of phase water(oil). Two phase velocities are given by Darcy's law:

$$\boldsymbol{v}_o = -\frac{\boldsymbol{k}k_{ro}}{\mu_o}\nabla p_o \tag{3}$$

$$\boldsymbol{v}_w = -\frac{\boldsymbol{k}k_{rw}}{\mu_w}\nabla p_w \tag{4}$$

where $p_{w(o)}$ is the pressure of water(oil), $k_{rw(o)}$ is the relative permeability of water(oil), and $\mu_{w(o)}$ is the viscosity of water(oil), $\boldsymbol{k}$ is absolute permeability tensor. Microscopic permeability of each grid is set as isotropic. The saturation and pressure are constrained by:

$$S_w + S_o = 1 \tag{5}$$

$$p_o - p_w = p_c(S_w) \tag{6}$$

where p_c is the capillary pressure. Initial and boundary conditions are set as:

$$S_w(x, y, t = 0) = S_{wr} \tag{7}$$

$$p_w(inlet, t) = p_0 \tag{8}$$

$$\nabla \cdot v_w|_\Gamma = 0 \tag{9}$$

where S_{wr} is the initial or residual water saturation of the model, p_0 is the constant pressure boundary at the inlet, Γ is the boundary other than the inlet.

Numerical experiment setup.

Numerical simulation is conducted using MATLAB Reservoir Simulation Toolbox (MRST) (Krogstad et al. 2015). We consider the usual power law correlations for the capillary pressure and relative permeability curves (Brooks and Corey 1963):

$$p_{cl} = p_b \left(S_o^{eff}\right)^a \tag{10}$$

$$k_{rwl} = k_{rwl}^0 \left(S_w^{eff}\right)^{n_{wl}} \tag{11}$$

$$k_{rol} = k_{rol}^0 \left(S_o^{eff}\right)^{n_{ol}} \tag{12}$$

where l indicates the matrix ($l = m$) or the micro-fractures ($l = f$). p_b is the threshold entry pressure, k_{rwl}^0 and k_{rol}^0 are the end points of the water and oil phase relative permeabilities in matrix or fracture, respectively. a, n_{wl} and n_{ol} are the capillary pressure, water phase relative permeability, and oil phase relative permeability exponent, respectively. S_w^{eff} and S_o^{eff} are the effective saturations of water and oil, respectively. In our simulation, $a = 2$ (Goda and Behrenbruch 2004). The effective saturations are normalized as:

$$S_w^{eff} = \frac{S_{wl} - S_{wrl}}{1 - S_{orl} - S_{wrl}} \tag{13}$$

$$S_o^{eff} = \frac{1 - S_{wl} - S_{orl}}{1 - S_{orl} - S_{wrl}} \tag{14}$$

where S_{wl} is the water saturation of matrix or micro-fractures, S_{wrl} and S_{orl} are the residual saturations of water and oil in the matrix or the micro-fractures, respectively. Additionally, for various micro-fracture apertures and matrix permeabilities, we apply the Leverett J-function (Leverett 1940) $p_c = \sigma\sqrt{\frac{\phi}{k}}J(S_w)$ to rescale the p_b values. We apply $k_f \propto b^2$ (assuming $k_f = 100$ mD with aperture of 0.03mm) (Gou et al. 2019) to rescale fracture permeability. **Table 1** and **Table 2** present the parameter values we adopt in the work, while **Fig. 3** illustrates the capillary pressure and relative permeability curves for matrix of $k_m = 0.0001$ mD, and micro-fractures with aperture of 0.03mm. ϕ_l is the porosity of matrix or micro-fractures.

b (mm)	k_f (mD)	p_b (Pa)
0.03	100	1.46×10^4
0.02	44.44	2.19×10^4
0.01	11.11	4.38×10^4
0.0075	6.25	5.85×10^4
0.005	2.78	8.77×10^4
0.0025	0.69	1.75×10^5

Table 1—Micro-fracture apertures and related permeabilities and threshold entry pressures.

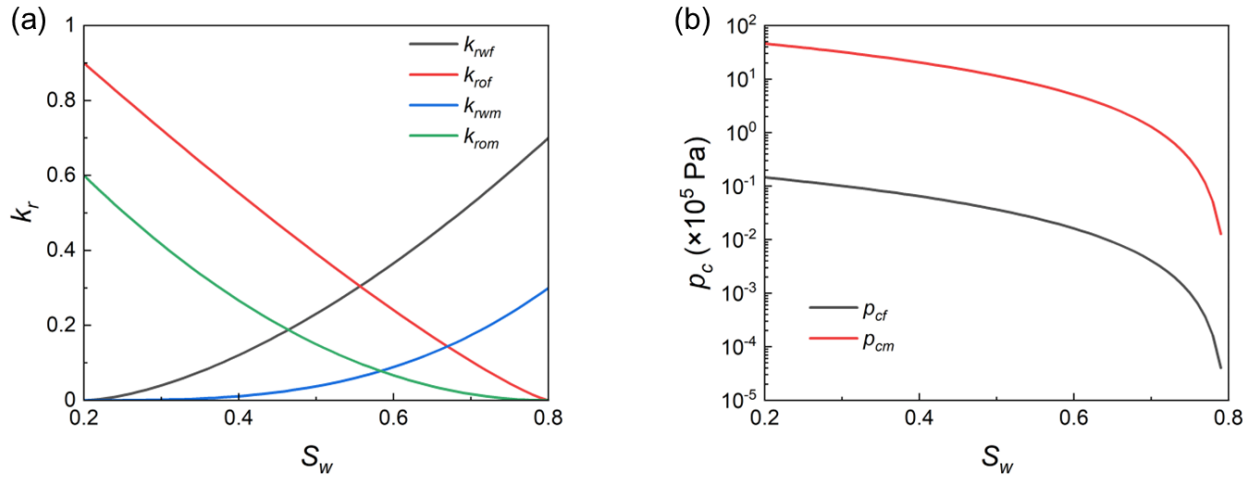| Medium	S_{wrl}	S_{orl}	k_{rwl}^0	k_{rol}^0	n_{wl}	n_{ol}	ϕ_l	k_l (mD)
Fracture	0.2	0.2	0.7	0.9	1.6	1.2	0.5	0.69-100
Matrix	0.2	0.2	0.3	0.6	3	2	0.05	0.01-0.0001

Table 2—General parameters for simulation.

Fig. 3—Relative permeability and capillary pressure curves of micro-fracture and matrix, b = 0.03 mm, k_m = 0.0001 mD. (a) Relative permeability curves; (b) Capillary pressure curves.

III. X-Direction Countercurrent Imbibition: Analysis and Theory

We first investigate unidirectional countercurrent imbibition parallel to the micro-fractures. There are two symmetric micro-fractures in the x-direction model (see **Fig. 2a**). The left side of the model is the water inlet and oil outlet with constant pressure. We demonstrate in **Fig. S-6a** and **Fig. S-7a** that mild asymmetry in micro-fractures does not affect the ultimate oil recovery. Therefore, we only present the imbibition in systems with symmetric micro-fractures. The effects of micro-fracture aperture, matrix permeability, oil viscosity, micro-fracture spacing on the cumulative oil production (Q) are studied. Additionally, a theoretical correlation of cumulative oil production is given, which is tested by comparing it with the fine grid simulation results. In comparison, the DP model with the same parameters as fine grid model is also simulated.

Demonstration of imbibition process.

In the demonstrative simulation, we set micro-fracture aperture, matrix permeability, oil viscosity, micro-fracture spacing as 0.03 mm, 0.0001 mD, 1 mPa·s and 0.24 mm, respectively. The water saturation distribution at three different time point during the countercurrent imbibition process of the x-direction model is shown in **Fig. 4a, b, c**. The cumulative oil production curve, presented on a log-log coordinate system, is shown in **Fig. 4d**.
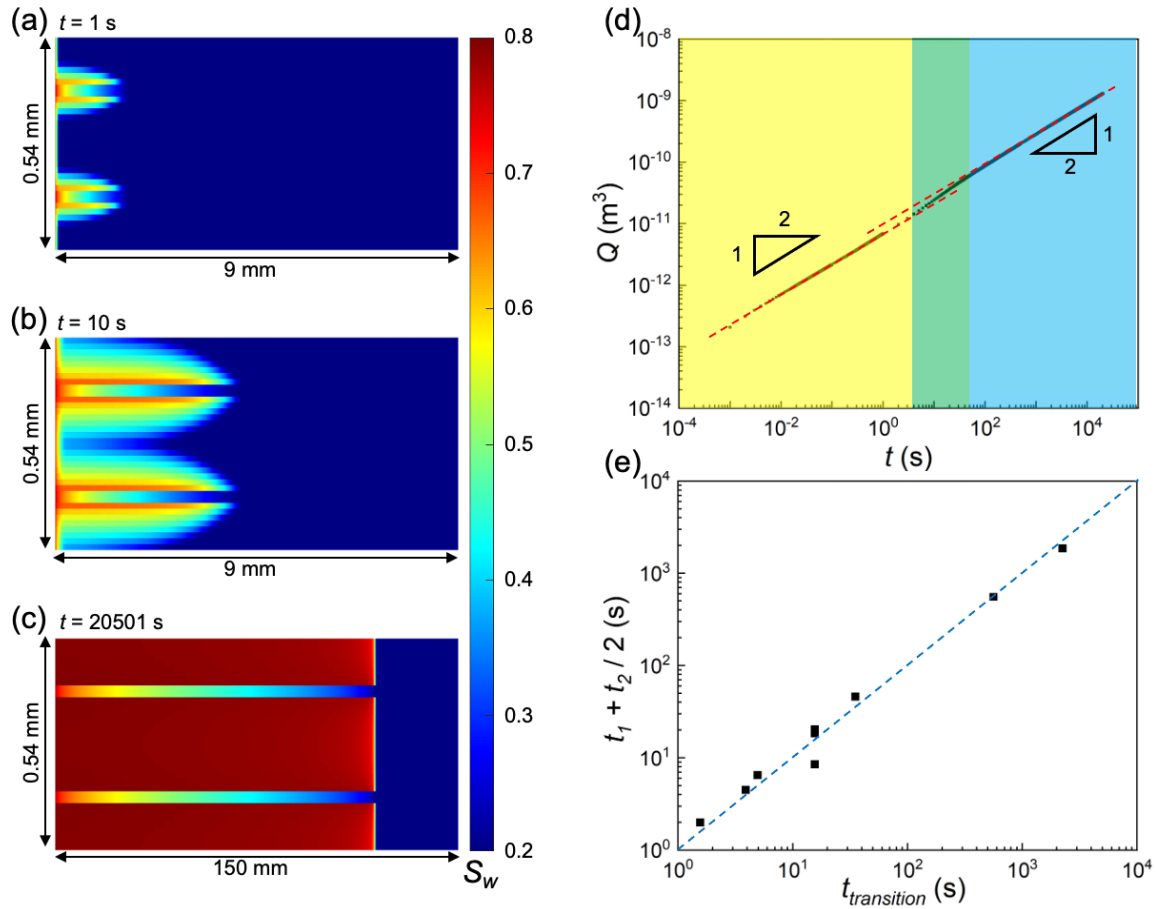
Fig. 4—Demonstration of x-direction model, $b = 0.03$ mm, $k_m = 0.0001$ mD, $\mu_o = 1$ mPa·s, $B = 0.24$ mm. (a) Details of water saturation distribution in early stage ($t = 1$ s); (b) Details of water saturation distribution between the early stage and the late stage ($t = 10$ s); (c) Water saturation distribution in late stage ($t = 20501$ s), red - high water saturation, blue - low water saturation. (d) Cumulative oil production curve with imbibition time in log-log coordinate, the x-axis is the imbibition time (t), the y-axis is the cumulative oil production (Q), the red dash line represents the cumulative oil production proportional to square root of imbibition time ($Q \propto t^{1/2}$) with different pre-factors; (e) comparison between arithmetic average $t_1 + t_2 / 2$ in the simulation and the theoretical transition time $t_{transition}$ in x-direction, the blue dash line is $y = x$.

Two distinct periods can be identified during the imbibition process:

Early stage. At the beginning of imbibition, fluid distribution around two micro-fractures are independent. Water preferentially enters the micro-fractures and simultaneously displaces near-fracture oil, and time is not enough for imbibed regions near two micro-fractures to overlap. Saturation gradient (thus the capillary pressure gradient) perpendicular to the micro-fractures in the matrix is very significant (**Fig. 4a**). This stage, where imbibition occurs in porous media with an independent fracture, has been extensively studied by numerous scholars (Andersen 2019; Andersen, Evje, and Kleppe 2014; Velasco-Lozano and Balhoff 2021). The early stage can be as short as ~1s, which is also much shorter than t_m (~10s) so DPF definition does not apply. Such short time period is practically negligible for shale oil recovery.

Late stage. The flows of two micro-fractures are highly synchronized and correlated. As the influenced regions from two micro-fractures gradually expand, they eventually contact and overlap with each other (**Fig. 4b**), and ultimately merge completely (**Fig. 4c**). The merging of two imbibed regions implies that the two micro-fractures have been coupled by capillarity. In the late stage, the imbibition front becomes flat and catches up with the front in fracture, and the water saturation in the matrix around the micro-fracture quickly reaches the maximum value when water front sweeps through. The late stage starts since 100 s in the demonstrative case, covering major time period of interest in oil recovery.

The transition from the early stage to the late stage thus corresponds to the time for water to fully saturate the matrix along y-direction, which can be estimated as $t_{transition} = \frac{B^2 \mu_w}{8 k_m \Delta p_{cm}}$ according to capillarity-driven Darcy's law, where Δp_{cm} is defined as the maximum capillary pressure contrast in the matrix, i.e., $p_{cm}(S_{wrm}) - p_{cm}(1 - S_{orm})$. In fine-grid simulation, the transition time can also be directly characterized by $(t_1 + t_2)/2$, where t_1 and t_2 are the beginning and end of the transition (rigorously defined in supplementary material). We measure $(t_1 + t_2)/2$ in multiple fine-grid simulations. As shown in **Fig. 4e**, the theoretical estimation ($t_{transition}$) can predict

numerical measurements $((t_1 + t_2)/2)$ very well. Detailed parameters of these fine-grid simulations are demonstrated in supplementary material (**Table S-1**).

Sensitivity analysis.

To investigate the impact of various factors on x-direction imbibition, we compare the production curves with six different micro-fracture apertures (0.03 mm, 0.02 mm, 0.01 mm, 0.0075 mm, 0.005 mm, 0.0025 mm), three different matrix permeabilities (0.0001 mD, 0.001 mD, 0.01 mD), six different oil or non-wetting phase viscosities (0.01 mPa·s, 0.1 mPa·s, 1 mPa·s, 20 mPa·s, 50 mPa·s, 100 mPa·s, while fixing the water or wetting phase viscosity at 1 mPa·s) and three micro-fracture densities (0.12 mm, 0.24 mm, 0.36 mm). The results are presented in **Fig. 5**.
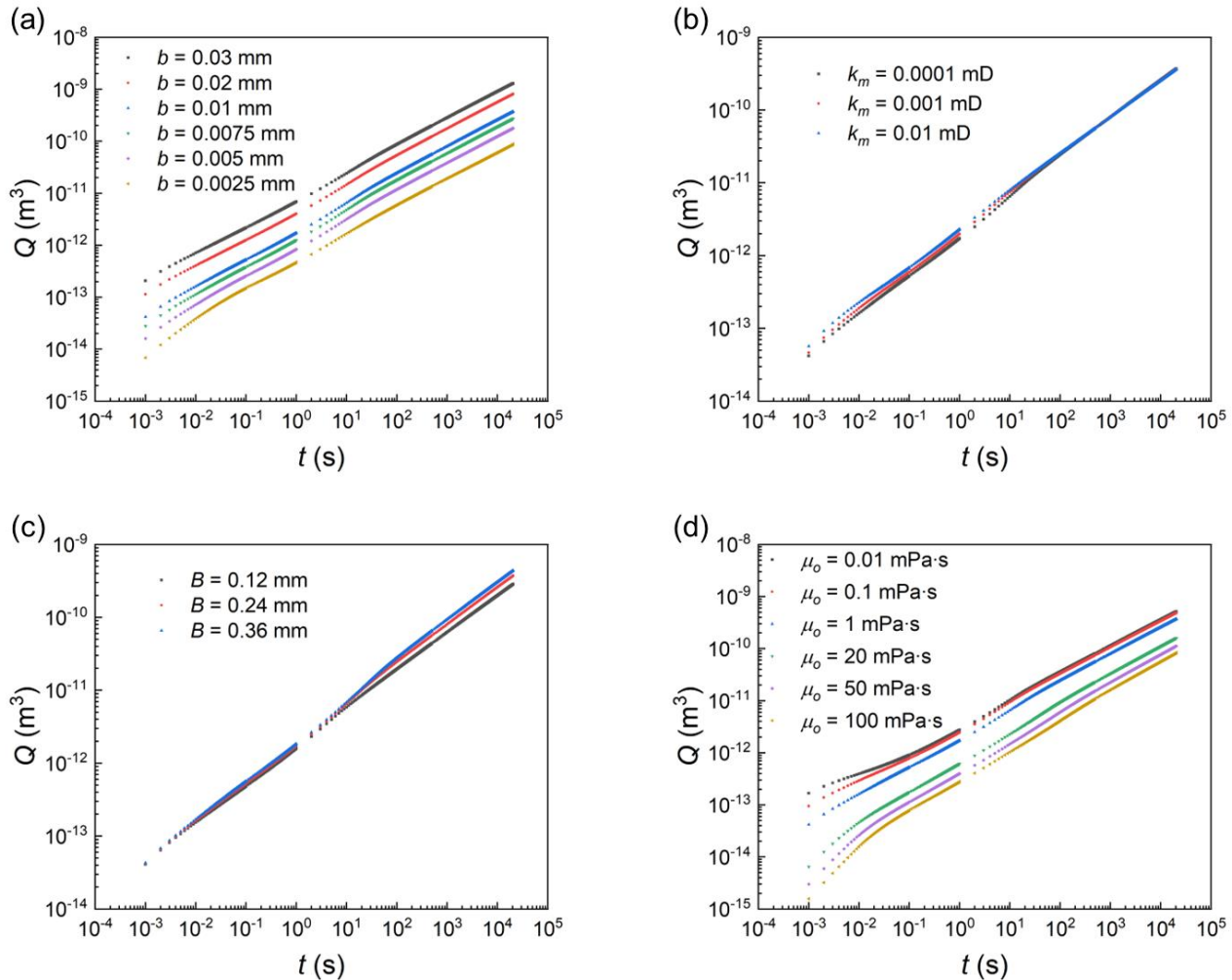
Fig. 5—Sensitivity analysis of cumulative oil production with different parameters, cumulative oil production curve with imbibition time in log-log coordinate, the x-axis is the imbibition time (t), the y-axis is the cumulative oil production (Q). (a) Cumulative oil production with different micro-fracture apertures (b), with k_m = 0.0001 mD, B = 0.24 mm, μ_o = 1 mPa·s; (b) Cumulative oil production with different matrix permeabilities (k_m), with b = 0.01 mm, B = 0.24 mm, μ_o = 1 mPa·s; (c) Cumulative oil production with different micro-fracture densities (B), with k_m = 0.0001 mD, b = 0.01 mm, μ_o = 1 mPa·s; (d) Cumulative oil production with different oil or non-wetting phase viscosities (μ_o), with k_m = 0.0001 mD, b = 0.01 mm, B = 0.24 mm.

In **Fig. 5a**, the influence of micro-fracture aperture (b) is illustrated, with the matrix permeability fixed at 0.0001 mD, the oil viscosity fixed at 1 mPa·s and the micro-fracture spacing fixed at 0.24 mm. Larger fracture aperture corresponds to higher cumulative oil production. In **Fig. 5b**, the influence of matrix permeability (k_m) is illustrated, with the micro-fracture aperture fixed at 0.01 mm, the oil viscosity fixed at 1 mPa·s and the micro-fracture spacing fixed at 0.24 mm. The simulation results reveal some differences in Q during the early stage. However, the late stage is barely affected by changing k_m. **Fig. 5c** illustrates the effect of micro-fracture spacing (matrix width between neighboring micro-fractures B), with the matrix permeability fixed at 0.0001 mD, the oil viscosity fixed at 1 mPa·s and the micro-fracture aperture fixed at 0.01 mm. Larger B (thicker matrix width) corresponds to higher Q. **Fig. 5d** presents cases

involving different oil viscosities, with the matrix permeability fixed at 0.0001 mD, the micro-fracture spacing fixed at 0.24 mm and the micro-fracture aperture fixed at 0.01 mm. Higher crude oil viscosity increases resistance to imbibition, resulting in a lower Q, as expected.

The fact that imbibition kinetics are insensitive to matrix permeability k_m indicates that the matrix contributes little to flow resistance in the late imbibition stage. The role of matrix in x-direction imbibition here is mainly to provide oil storage space. Therefore, the Darcy flow assumption in the matrix (assumption no.6) can be relaxed in a DPF system during x-direction imbibition.

Brief observation summary for countercurrent imbibition in x-direction.

1. In the early stage, fluid flows in neighboring micro-fractures are independent from each other, and the cumulative oil production is proportional to the square root of imbibition time ($Q \propto t^{1/2}$).

2. In the late stage, the imbibition fronts around neighboring micro-fractures merge into a synchronized flat front. In the late imbibition period, the cumulative oil production is also proportional to the square root of imbibition time ($Q \propto t^{1/2}$), but with a higher pre-factor than the early imbibition stage.

3. In the late stage, larger micro-fracture aperture (b), thicker matrix width (B, larger distance between neighboring micro-fractures) and lower oil viscosity result in higher oil production, while matrix permeability does not affect the ultimate imbibition kinetics.

Analytical solution for the late stage of countercurrent imbibition in x-direction modeling.

We have discussed that the late stage is the major stage that we concern in DPF systems. During the late stage, as the imbibition time into matrix (t_m) is significantly shorter than the imbibition time along the micro-fracture (t_f), we can assume that the fluid exchange between the micro-fractures and the surrounding matrix completes almost immediately at the imbibition front. It can be further demonstrated that the leading front of imbibition in the matrix aligns with the micro-fractures during the late imbibition period, as shown in **Fig. 4c**. In other words, we can assume that micro-fractures and the matrix achieve local capillary equilibrium at any given time throughout the late imbibition period. Therefore, the following relation holds:

$$p_{cf}(S_{wf}) = p_{cm}(S_{wm}) \tag{15}$$

where p_{cf} and p_{cm} are functions of the water saturation in the micro-fracture (S_{wf}) and matrix (S_{wm}), respectively.

It can be inferred from significant contrast between capillary pressure curves in the micro-fracture and in the matrix, that local capillary equilibrium regulates the matrix water saturation at the late stage as either close to the residual water saturation (extremely high capillary pressure, ahead imbibition front), or nearly saturated with wetting phase (low capillary pressure, swept region), while water saturation in the micro-fractures varies continuously. This inference is supported by numerical results (**Fig. 4c** and **Fig. 6**).
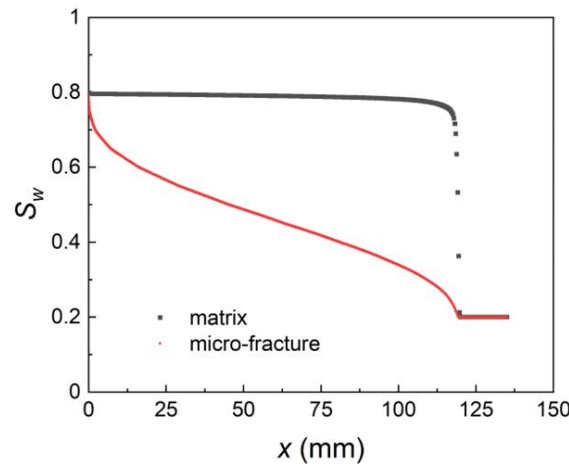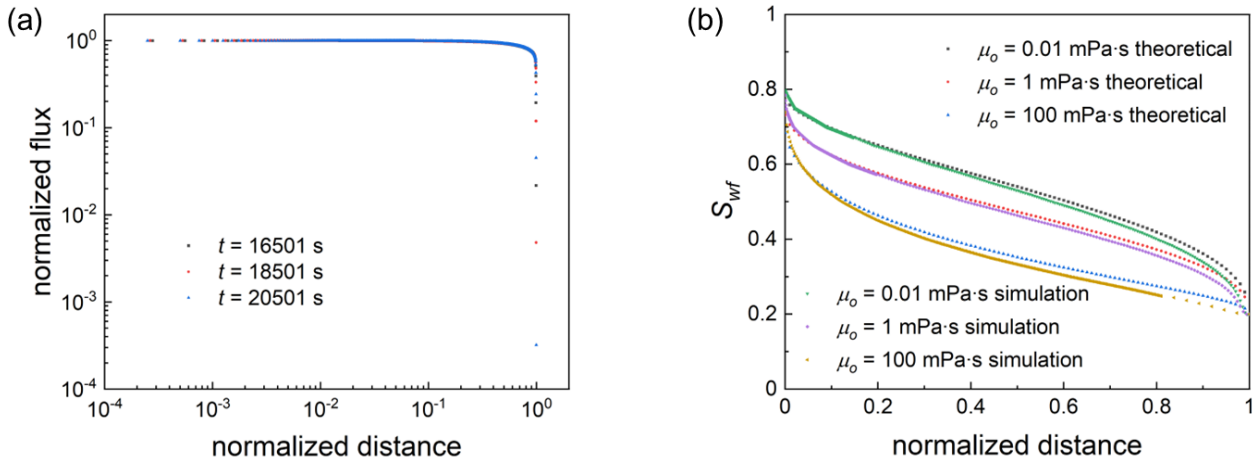

Fig. 6—Water saturation along the micro-fracture versus imbibition distance in normal coordinate, the x-axis is the imbibition distance, the y-axis is the water saturation (S_w), the red line represents the micro-fracture, the black line represents the matrix. Here we take the micro-fracture aperture as 0.03 mm, matrix permeability as 0.0001 mD, oil viscosity as 1 mPa·s and micro-fracture spacing as 0.24 mm for example, and capture the saturation profile at 20501s.

Therefore, we can assume that no further water enters the matrix after behind imbibition front, while the accumulation in the micro-fracture is very slow. This assumption is validated in **Fig. 7a** where the flux along the fracture at t = 16501 s, 18501 s, 20501s (the imbibition distance and flux are scaled to the range of [0 1]) overlap and varies little except near the imbibition front. We thus have

$$\frac{d}{dx}\left[\frac{k_f\lambda_{wf}\lambda_{of}dp_{cf}}{(\lambda_{wf}+\lambda_{of})dS_{wf}}\frac{dS_{wf}}{dx}\right]=0 \tag{16}$$

where $\lambda_{of}=k_{rof}/\mu_o$ and $\lambda_{wf}=k_{rwf}/\mu_w$ are the relative mobilities of oil and water phase in micro-fractures, respectively. By substituting the capillary pressure function and the relative permeability function into the **Eq. 16** above and simplifying, we eventually arrive at the following non-linear differential equation with respect to S_{wf}:

$$\frac{d}{dx}\left[\frac{\left(S_{wf}-S_{wrf}\right)^{n_{wf}}\times\left(1-S_{wf}-S_{orf}\right)^{n_{of}+a-1}}{\mu_o k_{rwf}^0\left(\frac{S_{wf}-S_{wrf}}{1-S_{orf}-S_{wrf}}\right)^{n_{wf}}+\mu_w k_{rof}^0\left(\frac{1-S_{wf}-S_{orf}}{1-S_{orf}-S_{wrf}}\right)^{n_{of}}}\times\frac{dS_{wf}}{dx}\right]=0 \tag{17}$$

Fig. 7—Spatial distribution of flux and water saturation along the micro-fracture during imbibition along x-direction. Here the spatial distance is the distance from the inlet normalized by front location, and the flux is normalized by the inlet flux. (a) Normalized flux along the micro-fracture versus normalized distance in three different time at the late stage in log-log coordinate. (b) Water saturation along the micro-fracture versus normalized distance in three different oil viscosities under theoretical and simulation conditions, plotted in normal coordinates, the x-axis represents the normalized distance, the y-axis represents the water saturation along the micro-fracture.

The distribution of S_{wf} at t = 20501 s for three different oil viscosities with the same micro-fracture aperture (0.01 mm), matrix permeability (0.0001 mD), and micro-fracture spacing (0.24 mm) is obtained using the Runge-Kutta method and the shooting method, as shown in **Fig. 7b**. The theoretical solutions align well with the numerical simulation results. Consequently, mean water saturation in the micro-fracture ($\overline{S_{wf}}$) can be determined from the distribution of water saturation along the micro-fracture direction in the late imbibition period. Subsequently, mean water saturation in the matrix ($\overline{S_{wm}}$) can be obtained from **Eq. 15**.

As discussed above, micro-fractures serve as the primary channels for imbibition in the late stage and contributes to major flow resistant, according to the simulation results. Therefore, Darcy's law can be simply adopted along the micro-fracture to calculate the fluid imbibition velocity of the whole DPF system along x-direction. Simultaneously, micro-fractures continuously distribute wetting fluid to the matrix at the imbibition front, so the mass stored in the matrix should be considered to modify the flow rate at the imbibition front. Therefore, the velocity of imbibition front position (denoted by L) can be expressed as:

$$\frac{dL}{dt}=-\frac{\beta k_f}{\overline{S_{wf}}\phi_f}\frac{\lambda_{of}\lambda_{wf}}{\lambda_{wf}+\lambda_{of}}\frac{\Delta p_{cf}}{L} \tag{18}$$

Here $\beta=\frac{V_{\phi f}\overline{S_{wf}}}{V_{\phi f}\overline{S_{wf}}+V_{\phi m}\overline{S_{wm}}}$ is the transition factor from water velocity in micro-fracture to front velocity where $V_{\phi f}$, $V_{\phi m}$ represent the pore volume of micro-fracture and matrix; $\overline{S_{wf}}\phi_f$ is the transition factor from water actual velocity to Darcy velocity along the micro-fracture; $\Delta p_{cf}=p_{cf}(S_{wf}=S_{wrf})-p_{cf}(S_{wf}=1-S_{orf})$ is the total capillary driving force along the micro-fracture. L is thus solved as:

$$L = \sqrt{\frac{2\beta}{\overline{S_{wf}}\phi_f} \frac{k_f \lambda_{o_f}(\overline{S_{wf}})\lambda_{w_f}(\overline{S_{wf}})}{\lambda_{o_f}(\overline{S_{wf}}) + \lambda_{w_f}(\overline{S_{wf}})} \Delta p_{cf}} \times \sqrt{t} \tag{19}$$

Therefore, the theoretical formula for cumulative oil production corresponding to any time t in the late stages:

$$Q = L \times \left[\phi_f A_f (\overline{S_{wf}} - S_{wrf}) + \phi_m A_m (\overline{S_{wm}} - S_{wrm})\right] \tag{20}$$

where A_f and A_m are the cross-sectional areas of micro-fracture and matrix.

To validate the theoretical correlation, we calculate the theoretical cumulative production at $t = 20501$ s for different micro-fracture apertures, different matrix permeabilities, different oil viscosities and different micro-fracture densities (results shown in **Fig. 8**). This theoretical cumulative production is proven to be in good agreement with the simulation results.
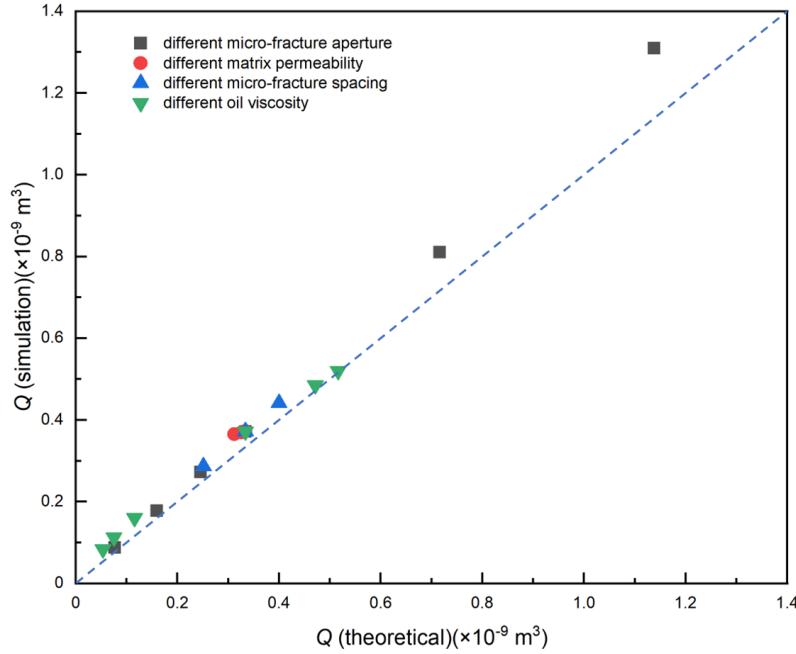

Fig. 8—Comparison between theoretical cumulative production and simulated cumulative production in different parameters, the blue dash line represents $y = x$.

Failure of DP model in x-direction imbibition.

We test the applicability of DP model in DPF system. The details of classical DP model and variables' setup are provided in the supplementary material (section S.V and **Fig. S-8**). We simulate two cases ($B = 0.24$ mm and 0.12 mm) with $k_m = 0.0001$ mD, $b = 0.01$ mm, and $\mu_o = 1$ mPa·s, with both fine grid model and DP model. The simulated cumulative oil productions are shown in **Fig. 9a**. In the early stage, DP model aligns well with the fine grid model. However, in the late stage, DP model significantly overestimates the oil production. In addition, we note that DP model overestimates the cumulative oil production by 151% for case $B = 0.24$ mm, while by 88% for case $B = 0.12$ mm, which are very different. This difference implies that the overestimation cannot be fixed by simply adjusting the fluid exchange constant in DP model (i.e., shape factor defined by Kazemi et al. (1976)). There must be failure of some fundamental assumption(s).

Classic DP models assume that averaged "matrix saturation" can be used to depict the local hydrodynamic features (capillary pressure, relative permeabilities, etc.) of the matrix. This assumption requires self-similarity of spatial fluid distribution when matrix exchanges fluid with local microfracture. To examine the DP fracture-matrix fluid exchange assumptions in DPF system, we quantify the capillary pressure gradient and oil pressure gradient in the matrix near the matrix-fracture interface in the fine grid simulation, and compare them against matrix-fracture capillary pressure gradient predicted by the DP model. We plot them along the direction of micro-fracture as shown in Figure **Fig. 9b**.

In swept region far from the front, DP model underestimates this capillary pressure gradient; nevertheless, a simple modification with constant pre-factor may fix it. However, in near-front region, DP model significantly overestimate the capillary pressure gradient by many orders of magnitude. This overestimation cannot be fixed by simply modifying the pre-factor. We rationalize it by non-equilibrium fluid exchange near the front: major amount of fluid has been exchanged near the front before a self-similar spatial fluid distribution is established in the matrix. As fluid change mainly emerges near the front, DP model drastically overestimates total oil recovery.
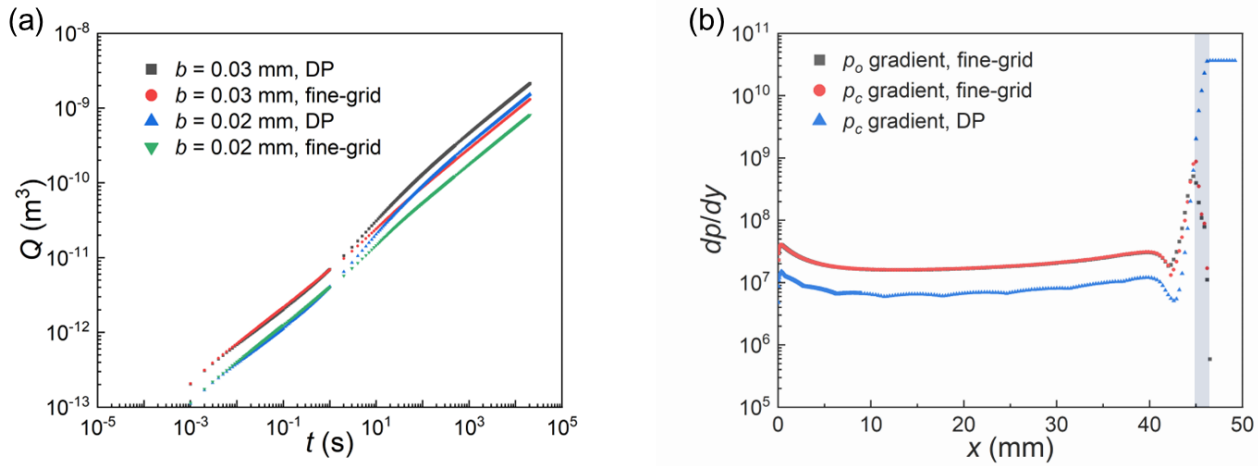
Fig. 9—Cumulative oil production of different micro-fracture densities and saturation profile in both the DP and fine grid models in x-direction. (a) Cumulative oil production in different micro-fracture densities, calculated by fine-grid model and by DP model, with fixed k_m = 0.0001 mD, b = 0.01 mm, and μ_o = 1 mPa·s, where DP model clearly overestimates the oil production; (b) The driving force of microfracture-matrix fluid exchange along x-direction, where dp/dy means the pressure gradient perpendicular to the micro-fracture in the matrix at the matrix-microfracture interface, the transparent blue rectangle indicates the water front region.

IV. Y-Direction Countercurrent Imbibition: Analysis and Theory

The y-direction countercurrent imbibition model grid setup is shown in **Fig. 2b**. The left side of the model is the water inlet and oil outlet with constant pressure, and the direction of imbibition is perpendicular to the micro-fracture extension direction. We also demonstrate in **Fig. S-6b** and **Fig. S-7b** that mild asymmetry in micro-fractures does not affect the ultimate oil recovery. Therefore, we only present the imbibition in systems with the same distance between neighboring two micro-fractures. The effects of micro-fracture aperture, matrix permeability, micro-fracture spacing and oil viscosity on the cumulative oil production are also studied. A theoretical model is proposed, and the accuracy of the theoretical solution is verified by comparing the theoretical and simulated cumulative oil production results. DP model with the same parameters as fine grid model is also simulated for comparison.

Demonstration of imbibition process.

Fig. 10a, b, c shows the water saturation distribution at three different time points during the countercurrent imbibition process of the y-direction model. The micro-fracture aperture, matrix permeability, oil viscosity and micro-fracture spacing are set at 0.01 mm, 0.001 mD, 1 mPa·s and 0.24 mm, respectively. The cumulative oil production curve is shown in **Fig. 10d**, presented on a log-log coordinate system.
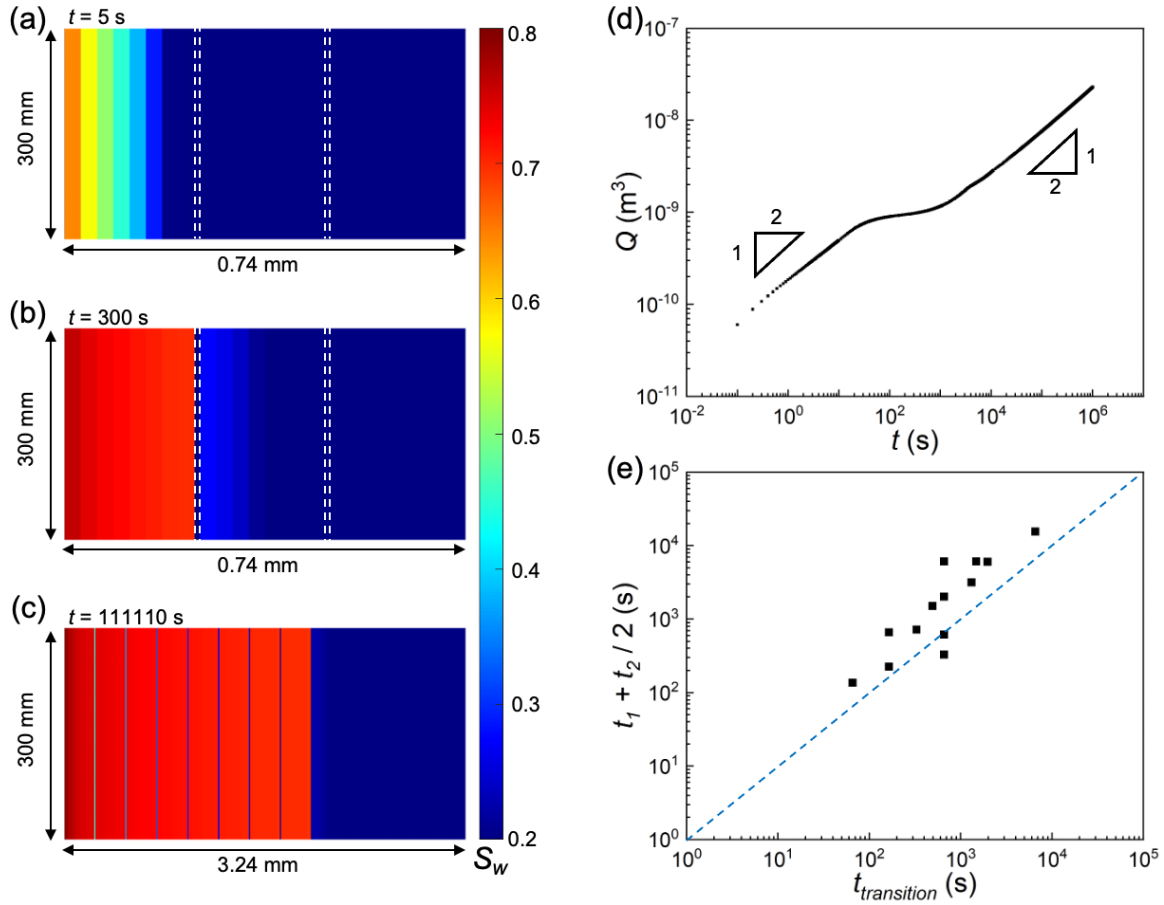
Fig. 10—Demonstration of y-direction model, b = 0.01 mm, k_m = 0.001 mD, μ_o = 1 mPa·s, B = 0.24 mm. (a) Details of water saturation distribution in early stage (t = 5 s), the white dash line is the first and second micro-fractures; (b) Details of water saturation distribution between the early stage and the late stage (t = 300 s), the white dash line is the first and second micro-fractures; (c) Water saturation distribution in late stage (t = 111110 s), red represents high water saturation, blue represents low water saturation, there are 12 micro-fractures, which could be seen 7 micro-fractures obviously. (d) Cumulative oil production curve with imbibition time in log-log coordinate, the x-axis is the imbibition time (t), the y-axis is the cumulative oil production (Q), the two triangles represents the cumulative oil production proportional to square root of imbibition time ($Q \propto t^{1/2}$) with different pre-factors; (e) comparison between arithmetic average $t_1 + t_2 / 2$ in the simulation and the theoretical transition time $t_{transition}$ in y-direction, the blue dash line is $y = x$.

Similar to x-direction imbibition, we also identify two distinct periods during y-direction imbibition:

Early stage. Water slowly saturates the first matrix block without penetrating the first micro-fracture. This is similar to the countercurrent imbibition into homogeneous media (**Fig. 10a**). The early stage can be as short as 30 s in the demonstrative case. At the end of the early stage, the water front meets the micro-fracture. However, as the capillary pressure in micro-fracture is much smaller than that in matrix, there is no adequate driving force for water to penetrate into the next matrix block. Therefore, the micro-fracture behaves like a closed boundary, while the average saturation in the first matrix block gradually increases towards its maximum. When the first matrix block reaches high water saturation, the imbibition driving force (capillary pressure gradient) becomes very small and the oil recovery significantly slows down, as shown in the plateau in **Fig. 10a**. When the first matrix block's water saturation further increases that the capillary pressure is comparable to that in the first micro-fracture, water start to flow into and across the first microfracture, and then into the second matrix block driven by the high capillary pressure

Late stage. The number of water-saturated matrix and micro-fractures is large enough. When the saturation in the first matrix block reaches almost the maximum and the capillary pressure decreases low enough, water is able to penetrate into the micro-fracture, and starts sweeping the next matrix block (**Fig. 10b**). As the imbibition progress deeper, the saturations in swept matrix blocks are all close to the maximum, while different micro-fractures have varying saturations (**Fig. 10c**). The late stage starts at 10000 s in the demonstrative case, which covers major time period of interest in oil recovery.

We note that the transition from the early stage to the late stage in y-direction imbibition also corresponds to the time for water to fully saturate the matrix along y-direction, similar to x-direction imbibition, except that the driving force is the capillary pressure contrast between different fractures. It thus can be estimated by $t_{transition} = \frac{B^2 \mu_w}{2k_m \Delta p_{cf}}$. Here, $\Delta p_{cf} = p_{cf}(S_{wrf}) - p_{cf}(1 - S_{orf})$. We measure ($t_1 +$

$t_2)/2$ in multiple fine-grid simulations for y-direction imbibition. As shown in **Fig. 10e**, the theoretical estimation ($t_{transition}$) can predict numerical measurements (($t_1 + t_2)/2$) very well. Detailed parameters of these fine-grid simulations are demonstrated in supplementary material (**Table S-2**).

Sensitivity analysis.

To investigate the impact of various factors on y-direction imbibition, six different micro-fracture apertures (0.03 mm, 0.02 mm, 0.01 mm, 0.0075 mm, 0.005 mm, 0.0025 mm), three different matrix permeabilities (0.0001 mD, 0.001 mD, 0.01 mD), three different oil or non-wetting phase viscosities (0.1 mPa·s, 1 mPa·s, 10 mPa·s, while fixing the water or wetting phase viscosity at 1 mPa·s) and three different micro-fracture densities (0.36 mm, 0.24 mm, 0.12 mm) are considered. The results are presented in **Fig. 11**.
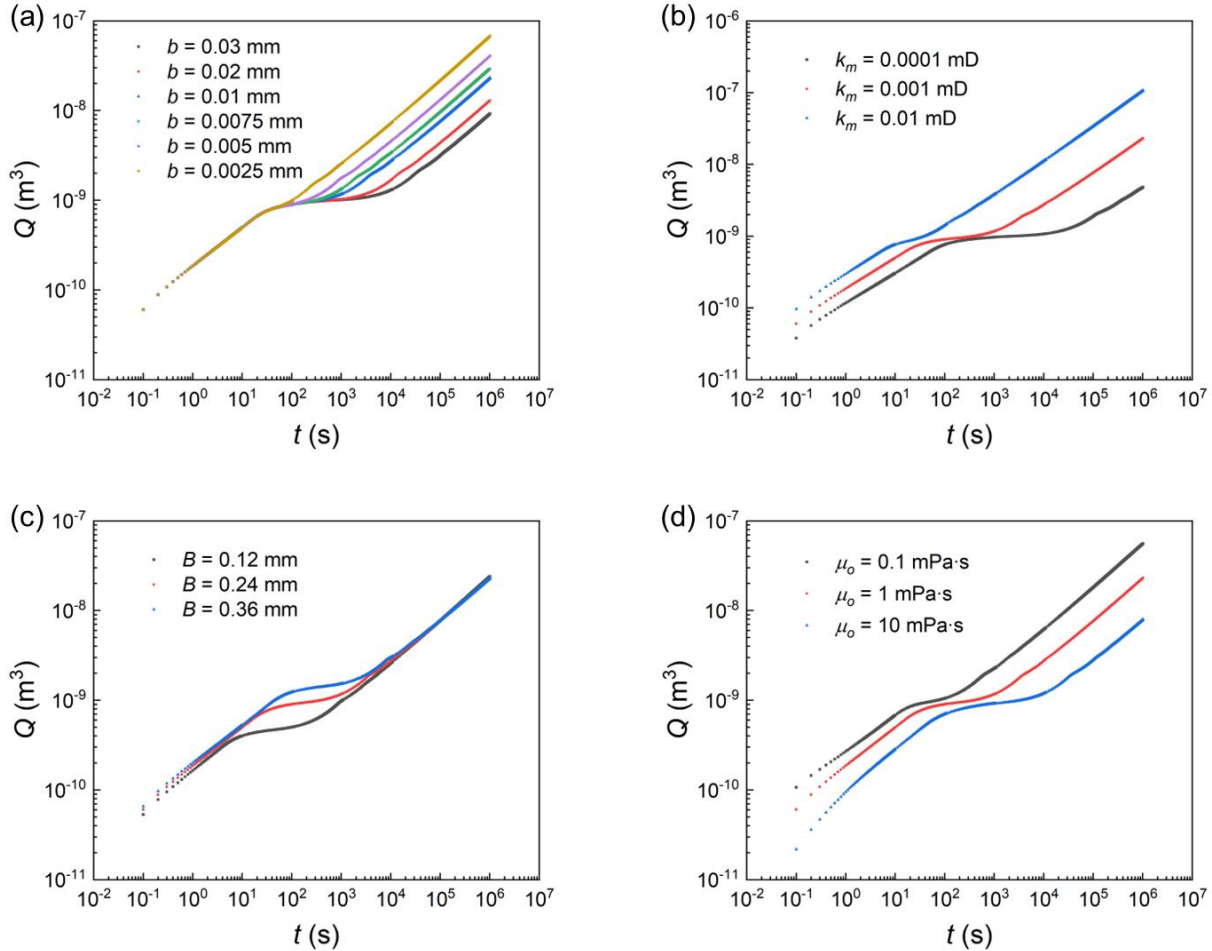
Fig. 11—Sensitivity analysis of cumulative oil production with different parameters, cumulative oil production curve with imbibition time in log-log coordinate, the x-axis is the imbibition time (t), the y-axis is the cumulative oil production (Q). (a) Cumulative oil production with different micro-fracture apertures (b), with k_m = 0.001 mD, B = 0.24 mm, μ_o = 1 mPa·s; (b) Cumulative oil production with different matrix permeabilities (k_m), with b = 0.01 mD, B = 0.24 mm, μ_o = 1 mPa·s; (c) Cumulative oil production with different micro-fracture densities (B), with b = 0.01 mD, k_m = 0.001 mD, μ_o = 1 mPa·s; (d) Cumulative oil production with different oil or non-wetting phase viscosities (μ_o), b = 0.01 mD, k_m = 0.001 mD, B = 0.24 mm.

In **Fig. 11a**, the influence of micro-fracture aperture (b) is illustrated, with the matrix permeability fixed at 0.001 mD, the oil viscosity fixed at 1 mPa·s and the micro-fracture spacing fixed at 0.24 mm. Larger micro-fracture aperture results in lower capillary pressure, which leads to slower penetration into the micro-fracture, thus resulting in lower Q in late stage. In **Fig. 11b**, the influence of matrix permeability (k_m) is illustrated, with the micro-fracture aperture fixed at 0.01 mm, the oil viscosity fixed at 1 mPa·s and the micro-fracture spacing fixed at 0.24 mm. The simulation results show that Q increases with k_m in the early stage, as the flow resistance is proportional to k_m, while the driving force is proportional to $k_m^{-1/2}$. The sensitivity of Q to k_m is largely amplified in late stage, which implies that the driving force may no longer be the capillary pressure in matrix. **Fig. 11c** illustrates the effect of micro-fracture spacing (matrix width between neighboring micro-fractures B), with the matrix permeability fixed at 0.001 mD, the micro-fracture aperture fixed at 0.01 mm and the oil viscosity fixed at 1 mPa·s. Larger B (thicker matrix width) only slightly changes the behavior of the transition between early and late stage, but has little effect on Q in both early and later stage. This insensitivity of B implies that the major resistance is not in the micro-fracture. In addition, **Fig. 11d** presents cases involving different oil viscosities, with the matrix permeability fixed at

0.001 mD, the micro-fracture aperture fixed at 0.01 mm and the micro-fracture spacing fixed at 0.24 mm. Higher crude oil viscosity increases resistance to imbibition, resulting in a poorer final recovery, as expected.

Brief summary of the countercurrent imbibition in y-direction.

1. The early stage of y-direction imbibition occurs in the first matrix block, and the cumulative oil production is initially proportional to the square root of imbibition time ($Q \propto t^{1/2}$), following classic model for countercurrent imbibition in homogeneous media.

2. In the late stage of imbibition, the cumulative oil production is proportional to the square root of imbibition time ($Q \propto t^{1/2}$), but with a smaller pre-factor than that in the early stage.

3. Smaller micro-fracture aperture, higher matrix permeability and lower viscosity contribute to oil production, while micro-fracture spacing does not impact the ultimate imbibition kinetics. We thus suspect that the resistance mainly occurs in matrix blocks, while the driving force is controlled by micro-fracture in the late stage.

Analytical solution for the late stage of countercurrent imbibition in y-direction modeling.

In the late stage y-direction imbibition, the matrix and micro-fractures also reach a capillary equilibrium as that in late stage x-direction imbibition, which can be described by the same equation as **Eq. 15**. Similarly, the capillary pressure in the micro-fractures is much smaller than the matrix capillary pressure corresponding to the same water saturation. Therefore, achieving equal capillary pressures is only possible if the water saturation in the matrix is close to the maximum or if both matrix and micro-fracture are at residual water saturation. In other words, the water saturation in the matrix at the late imbibition stage is either close to the maximum or equal to the residual water saturation, leading to two plateaus in the water saturation distribution curve, which is supported by **Fig. 12** at the late imbibition stage. Whereas, the micro-fracture water saturation varies continuously along the imbibition direction, which is in agreement with the conjecture that we have proposed.
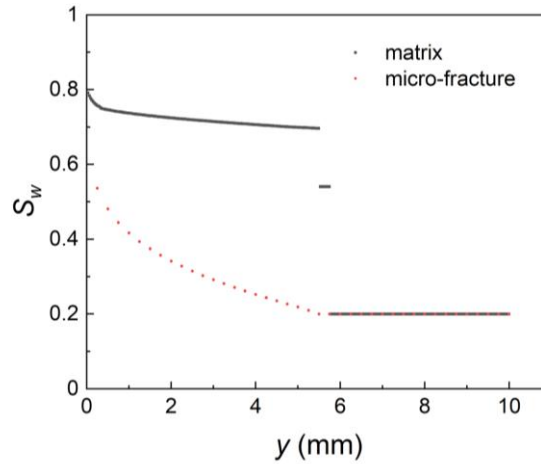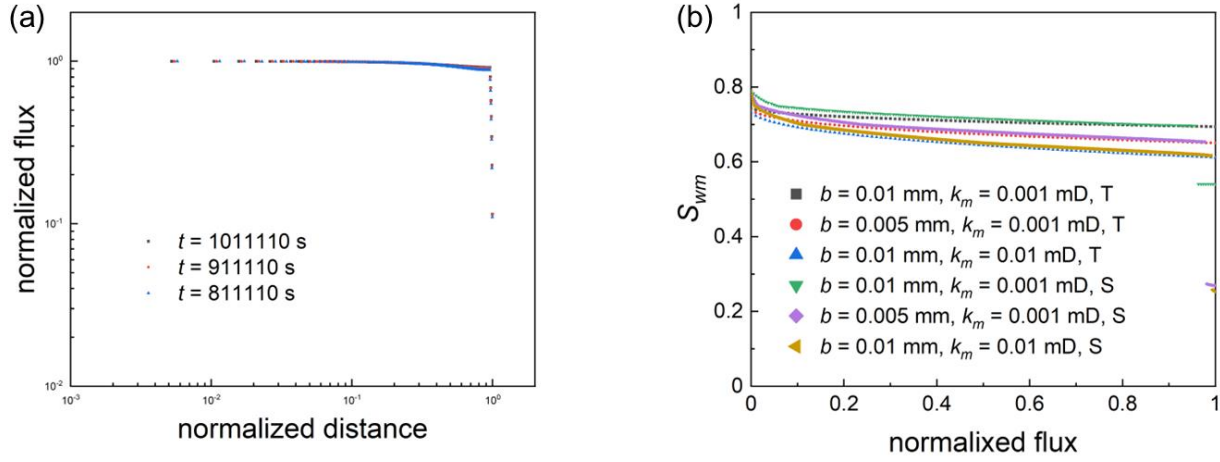

Fig. 12—Water saturation along the imbibition direction versus imbibition distance in normal coordinate, the x-axis is the imbibition distance, the y-axis is the water saturation (S_w), the red points represent different micro-fractures' water saturation, the black curve segments represent the matrix water saturation. We note that the black curve segments and red points are discontinuous.

Consequently, we can calculate the mean water saturation in the micro-fracture $(\overline{S_{wf}})$ from the known mean water saturation in the matrix $(\overline{S_{wm}})$ according to the capillary equilibrium formula by **Eq. 15**. **Fig. 13a** illustrates the variation curve of the water imbibition flux with imbibition distance along the imbibition direction at the late stage. It can be seen that the normalized flux at t = 811110 s, 911110 s, 1011110 s, the normalized flux along the imbibition direction is almost constant with a small variation. Since the flow resistance during the late stage of imbibition mainly occurs in the matrix and the driving force is regulated by capillary equilibrium, it is obtained from Darcy's law that:

$$\frac{d}{dx}\left[\frac{k_m \lambda_{wm} \lambda_{om} dp_{cm}}{(\lambda_{wm} + \lambda_{om}) dS_{wm}} \frac{dS_{wm}}{dx}\right] = 0 \tag{21}$$

where $\lambda_{om} = k_{rom}/\mu_o$ and $\lambda_{wm} = k_{rwm}/\mu_w$ are the relative mobility of oil and water phase in matrix, respectively. The relative permeability and capillary pressure function are substituted in **Eq. 21** and simplified:

$$\frac{d}{dx}\left[\frac{(S_{wm}-S_{wrm})^{n_{wm}} \times (1-S_{wm}-S_{orm})^{n_{om}+a-1}}{\mu_o k_{rwm}^0 \left(\frac{S_{wm}-S_{wrm}}{1-S_{orm}-S_{wrm}}\right)^{n_{wm}} + \mu_w k_{rom}^0 \left(\frac{1-S_{wm}-S_{orm}}{1-S_{orm}-S_{wrm}}\right)^{n_{om}}} \times \frac{dS_{wm}}{dx}\right] = 0 \tag{22}$$

Fig. 13—Spatial distribution of flux and water saturation during y-direction imbibition. Here the spatial distance is the distance from the inlet normalized by front location, and the flux is normalized by the inlet flux. **(a)** Normalized flux along the imbibition direction versus normalized distance in three different time at the late stage in log-log coordinate, the x-axis is the normalized distance, the y-axis is the normalized flux; **(b)** Matrix water saturation along the imbibition direction versus normalized distance in three different cases under theoretical and simulation conditions, plotted in normal coordinates, the x-axis represents the normalized distance, the y-axis represents the matrix water saturation along the imbibition direction, the oil viscosity in all the cases is 1 mPa·s, T represents theoretical, and S represents simulation.

The distribution of water saturation along the imbibition direction at $t = 1011110$ s for three different cases is obtained using the Runge-Kutta method and the shooting method, as shown in **Fig. 13b**. It is evident that the theoretical solution aligns well with the numerical simulation, affirming that the imbibition flux along the imbibition direction is uniform everywhere except at the front of imbibition. Consequently, $\overline{S_{wm}}$ can be determined from the distribution of water saturation along the imbibition direction in the late imbibition period. Subsequently, $\overline{S_{wf}}$ can be obtained from the **Eq. 15**.

We succeed in deriving the distribution of water saturation at any moment during the late stage of countercurrent imbibition in y-direction model. The imbibition flow occurs mainly in the matrix, thus the imbibition front velocity at the late stage is:

$$\frac{dL}{dt} = -\frac{k_m}{\overline{S_w}\phi_e}\frac{\lambda_{om}\lambda_{wm}}{\lambda_{wm}+\lambda_{om}}\frac{\Delta p_{cm}}{L} \tag{23}$$

Where ϕ_e is the averaged porosity between matrix and micro-fracture, and $\overline{S_w}$ is the averaged water saturation between matrix and micro-fracture. $\overline{S_w}\phi_e$ thus is the factor to transient Darcy velocity to actual water velocity. By utilizing the mean velocity formula, the position of the imbibition front (L) along the imbibition direction at imbibition time (t) is then determined as:

$$L = \sqrt{\frac{2}{\overline{S_w}\phi_e}\frac{k_m\lambda_{o_m}(\overline{S_{wm}})\lambda_{w_m}(\overline{S_{wm}})}{\lambda_{o_m}(\overline{S_{wm}})+\lambda_{w_m}(\overline{S_{wm}})}\Delta p_{cm}} \times \sqrt{t} \tag{24}$$

In the late imbibition period, capillary equilibrium yields $\Delta p_{cm}=\Delta p_{cf} = p_{cf}(S_{wrf}) - p_{cf}(1 - S_{orf})$. Therefore, the theoretical formula for cumulative oil production corresponding to any imbibition time t in the late stage is:

$$Q = L \times \left[\frac{b}{b+B} \times \phi_f A(\overline{S_{wf}} - S_{wrf}) + \frac{B}{b+B} \times \phi_m A(\overline{S_{wm}} - S_{wrm})\right] \tag{25}$$

where A is the cross-sectional area of y-direction model.

To validate the theoretical correlation, we can calculate the theoretical cumulative production at $t = 1011110$ s for different micro-fracture apertures, different matrix permeabilities, different oil viscosities and different micro-fracture densities (results shown in **Fig. 14**). This theoretical cumulative production is proven to be in good agreement with the simulation results.
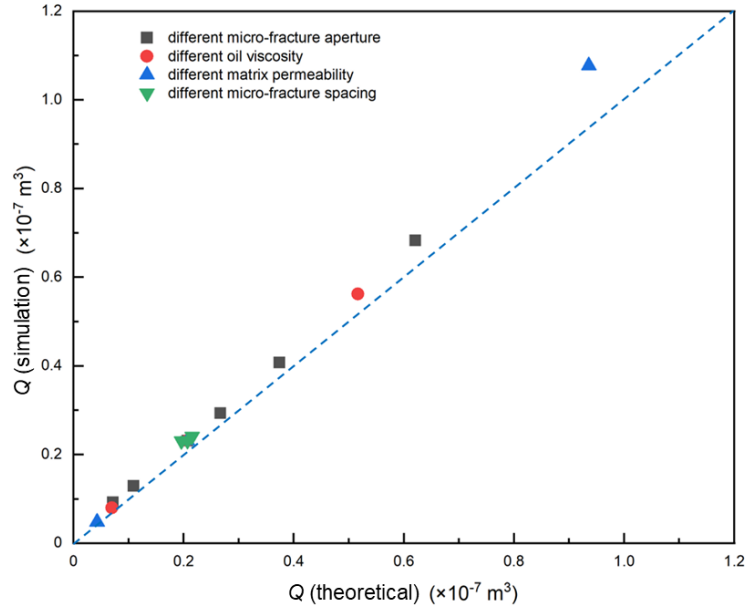
Fig. 14—Comparison between theoretical cumulative production and simulated cumulative production in different parameters, the blue dash line represents $y = x$.

Comparison of DP model in y-direction.

We also simulate the DP model in the y-direction for comparison, and the results are presented in **Fig. 15**. It is apparent that the cumulative oil production of the DP model does not align with that of the fine grid model.
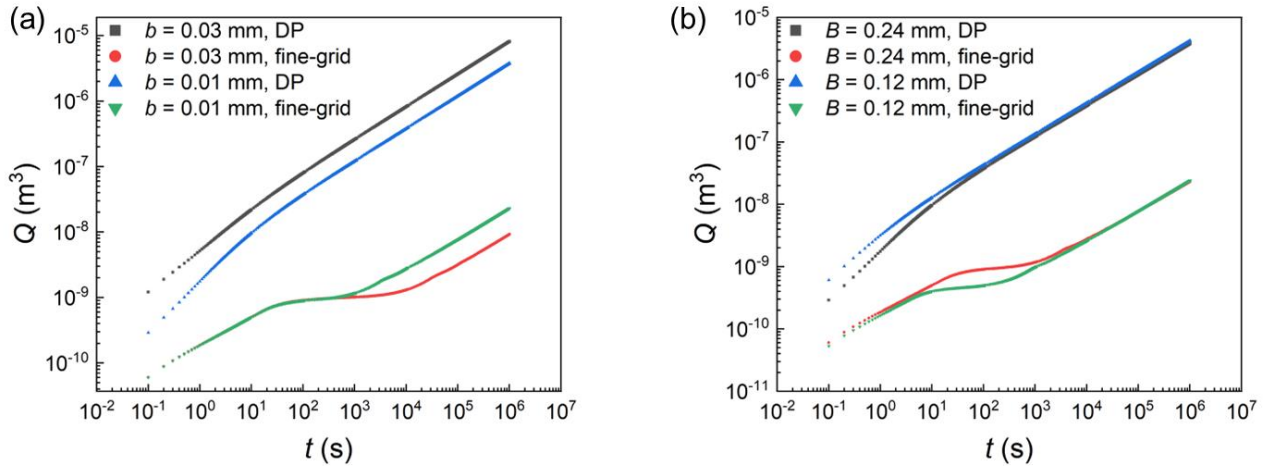

Fig. 15—Cumulative oil production of several cases in both the DP and fine grid models in y-direction. (a) Different micro-fracture apertures, with $k_m = 0.001$ mD, $B = 0.24$ mm, $\mu_o = 1$ mPa·s; (b) Different micro-fracture densities, with $b = 0.01$ mD, $k_m = 0.001$ mD, $\mu_o = 1$ mPa·s.

V. Equivalent REV Model

Although fine-grid simulation can provide good accuracy, using such small grid sizes (tens of microns) is computational not acceptable for reservoir simulation. To depict two phase flow in DPF systems in a practical reservoir simulator, developing an equivalent representative elementary volume (REV) scale model is necessary. As the early stage of imbibition is very short, we only consider the late stage. Subsequently, we validate the equivalent REV model using a 2-D imbibition case.

Equivalent porosity, absolute permeabilities and capillary pressure.

The porosity of the equivalent REV model (ϕ_e) is calculated as:

$$\phi_e = \gamma\phi_f + (1 - \gamma)\phi_m \tag{26}$$

where $\gamma = \frac{V_f}{V_f+V_m}$ is the percentage of the micro-fracture volume to the entire volume, V_f and V_m are the micro-fracture volume and matrix volume, respectively. The equivalent absolute permeability of x-direction model (K_x) can be calculated from the parallel connection formula:

$$K_x = \frac{bk_f + Bk_m}{b + B} \tag{27}$$

In the y-direction imbibition model, the matrix and micro-fractures are connected in series, and the equivalent absolute permeability of y-direction model (K_y) can be expressed as follows:

$$K_y = \frac{b + B}{\frac{b}{k_f} + \frac{B}{k_m}} \tag{28}$$

The equivalent water saturation (S_w) can be calculated as follows:

$$S_w = \omega S_{wf} + (1 - \omega)S_{wm} \tag{29}$$

Where $\omega = \frac{V_{\phi f}}{V_{\phi f}+V_{\phi m}}$.It is important to note that S_{wf} and S_{wm} are not independent variables. They are correlated due to the local capillary equilibrium between the micro-fractures and the matrix, as shown in **Eq. 15** for both the x-direction and y-direction.

Capillary pressure in a DPF system can be determined by combining **Eq. 15** and **Eq. 29**, and applying the constraint $S_{wf} \geqslant S_{wrf}$ to ensure that the capillary pressure cannot be larger than the maximum capillary pressure in the micro-fracture ($p_{cf}(S_{wrf})$). We define critical matrix water saturation (S_{wmc}) that $p_{cm}(S_{wmc}) = p_{cf}(S_{wrf})$. When $S_w \geqslant \omega S_{wrf} + (1-\omega) S_{wmc} = S_{wc}$ (here we use S_{wc} to define averaged critical water saturation of equivalent REV model), capillary pressure can be simply determined by combining **Eq. 15** and **Eq. 29**. When $S_w < \omega S_{wrf} + (1-\omega) S_{wmc} = S_{wc}$, the capillary pressure is set equal to $p_{cf}(S_{wrf})$, because in both x-direction and y-direction, the driving force is the capillary pressure in the micro-fracture in the late stage. The capillary pressure of the equivalent REV model is thus obtained, as shown in **Fig. 16a** (taking the micro-fracture aperture 0.01 mm, matrix permeability 0.001 mD, micro-fracture spacing 0.24 mm as an example).
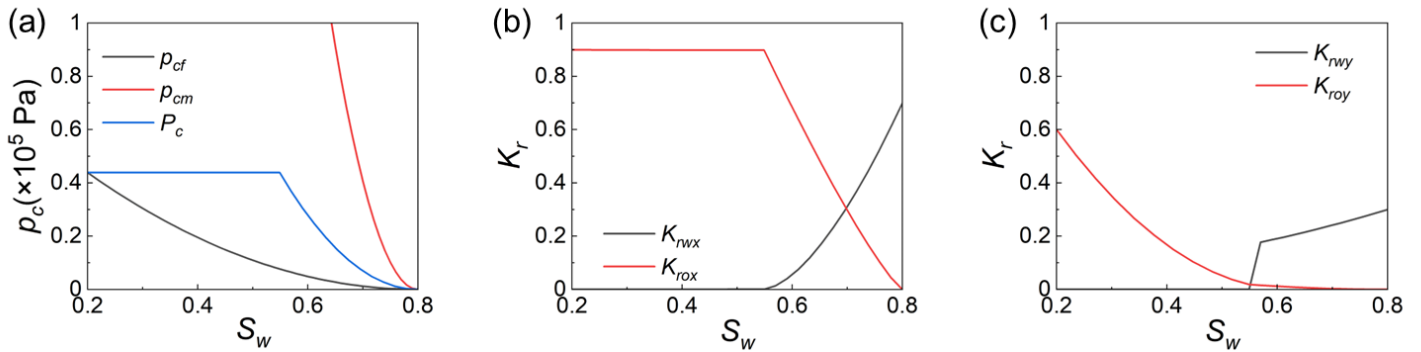
Fig. 16—Equivalent REV capillary pressure and anisotropic relative permeability curves. (a) Equivalent REV capillary pressure curve – black line, matrix (green line) and micro-fracture (red line) capillary pressure line; (b) Equivalent REV relative permeability curve along the micro-fracture direction (x-direction); (c) Equivalent REV relative permeability curve along the imbibition direction (y-direction). All curves in this figure adopt micro-fracture aperture 0.01 mm, matrix permeability 0.001 mD, micro-fracture spacing 0.24 mm as an example.

Equivalent anisotropic relative permeabilities.

Relative permeability in x-direction. As analyzed earlier, the flow resistance along the micro-fracture imbibition (x-direction) in a DPF system at late stage is mainly from micro-fracture, while the matrix's role is to store fluid. Therefore, the matrix can be neglected to impermeable layer when calculating the flow resistance with known flux. As the micro-fractures and the matrix are parallel to flow direction, the x-direction relative permeability can be calculated as:

$$K_{rwx} = \frac{bk_f k_{rwf}}{(b + B)K_x} \tag{30}$$

$$K_{rox} = \frac{bk_f k_{rof}}{(b + B)K_x} \tag{31}$$

Relative permeability in y-direction. In the y-direction imbibition model, the matrix and micro-fractures are connected in series. Thus, y-direction relative permeability can be calculated as:

$$K_{rwy} = \frac{b + B}{\left(\frac{b}{k_f k_{rwf}} + \frac{B}{k_m k_{rwm}}\right) K_y} \tag{32}$$

$$K_{roy} = \frac{b + B}{\left(\frac{b}{k_f k_{rof}} + \frac{B}{k_m k_{rom}}\right) K_y} \tag{33}$$

We note that the anisotropy exists not only in absolute permeability, but also in relative permeability. It aligns with some recent approaches on layered porous media (Pei et al. 2023; 2022; Keilegavlen, Nordbotten, and Stephansen 2012). Unfortunately, current commercial reservoir simulators only use anisotropic absolute permeability to depict anisotropy. As the relative permeabilities are of very different shapes in different directions for DPF systems, it becomes necessary to establish reservoir simulation technology that is compatible with the setting of anisotropic relative permeability.

Unidirectional validation of equivalent REV models.

We conduct numerical simulation using the equivalent REV model and compare the results with those of fine grid model simulation above mentioned. As shown in supplemental materials **Fig. S-9** and **Fig. S-10**, the late time results exhibit an excellent match.

In addition, we compare the REV simulation along x-direction (grid size 10 cm, total model length 5 m, simulation time 300 days) and y-direction (grid size 1 cm, total model length 1.5 m, simulation time 30000days) against our theoretical model (**Eq.20** and **Eq.25**), which both match very well, As shown in **Fig.17 a&b.** Here the REV model grid size is chosen to reach the minimum arid size in reservoir simulation.

We also simulate two different cases with more complex heterogeneity (Saif et al. 2017): 1) staggered distributed micro-fractures and 2) non-uniform micro-fractures. Simulation results show that the REV model for both x- and y- directions well matches the fine-grid simulations, as demonstrated in detail in supplementary materials (**Fig. S-11** and Fig. **S-12**).
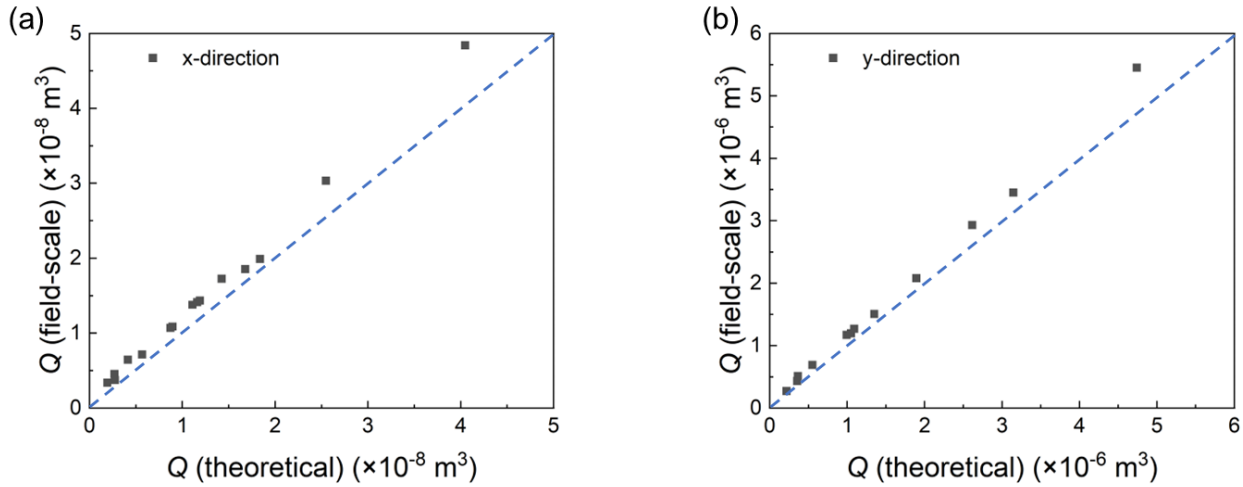
Fig. 17 Comparison of cumulative oil production between REV model in huge grids (field-scale) and theoretical model in x-direction and y-direction, the blue dash lines represent y = x. (a) Results in x-direction; (b) Results in y-direction.

Summary of equivalent REV model.

If the coordinate is selected that x-axis is parallel to the micro-fracture in a DPF system, the permeabilities, relative permeabilities and capillary pressure in 2-D system are as follows:

$$K = \begin{pmatrix} K_x & 0 \\ 0 & K_y \end{pmatrix} \tag{34}$$

$$K_{rw} = \begin{pmatrix} K_{rwx} & 0 \\ 0 & K_{rwy} \end{pmatrix} \tag{35}$$

$$K_{ro} = \begin{pmatrix} K_{rox} & 0 \\ 0 & K_{roy} \end{pmatrix} \tag{36}$$

$$P_c = \begin{cases} p_{cf}(S_{wrf}), S_w < S_{wc} \\ p_{bf}\left(\dfrac{1 - S_w - S_{or}}{1 - S_{wc} - S_{or}}\right)^a, S_w \geq S_{wc} \end{cases} \tag{37}$$

where p_{bf} is the threshold entry pressure of micro-fracture, S_{or} is the averaged residual oil saturation of equivalent REV model, which can be calculated by **Eq. 29**.

For 2-D system, the governing equation is shown below:

$$\phi_e \frac{\partial S_w}{\partial t} = \frac{\partial}{\partial x}\left(\frac{K_x \lambda_{wx} \lambda_{ox}}{\lambda_{wx} + \lambda_{ox}} \frac{\partial P_C}{\partial S_w} \frac{\partial S_w}{\partial x}\right) + \frac{\partial}{\partial y}\left(\frac{K_y \lambda_{wy} \lambda_{oy}}{\lambda_{wy} + \lambda_{oy}} \frac{\partial P_C}{\partial S_w} \frac{\partial S_w}{\partial y}\right) \tag{38}$$

where $\lambda_{wx} = \frac{K_{rwx}}{\mu_w}$, $\lambda_{wy} = \frac{K_{rwy}}{\mu_w}$, $\lambda_{ox} = \frac{K_{rox}}{\mu_o}$, $\lambda_{oy} = \frac{K_{roy}}{\mu_o}$.

Validation in oblique imbibition model.

Here we introduce a more practical model that the imbibition direction is neither parallel nor perpendicular to the direction of micro-fractures, from a point source at the corner (**Fig. 1c**). The fine grid simulation is conducted, and water saturation profile at $t = 1000000$ s is shown in **Fig. 18a**. We further average saturation in local micro-fractures and matrix blocks of the fine grid scale to get coarsened saturation profile as shown in **Fig. 18b**.
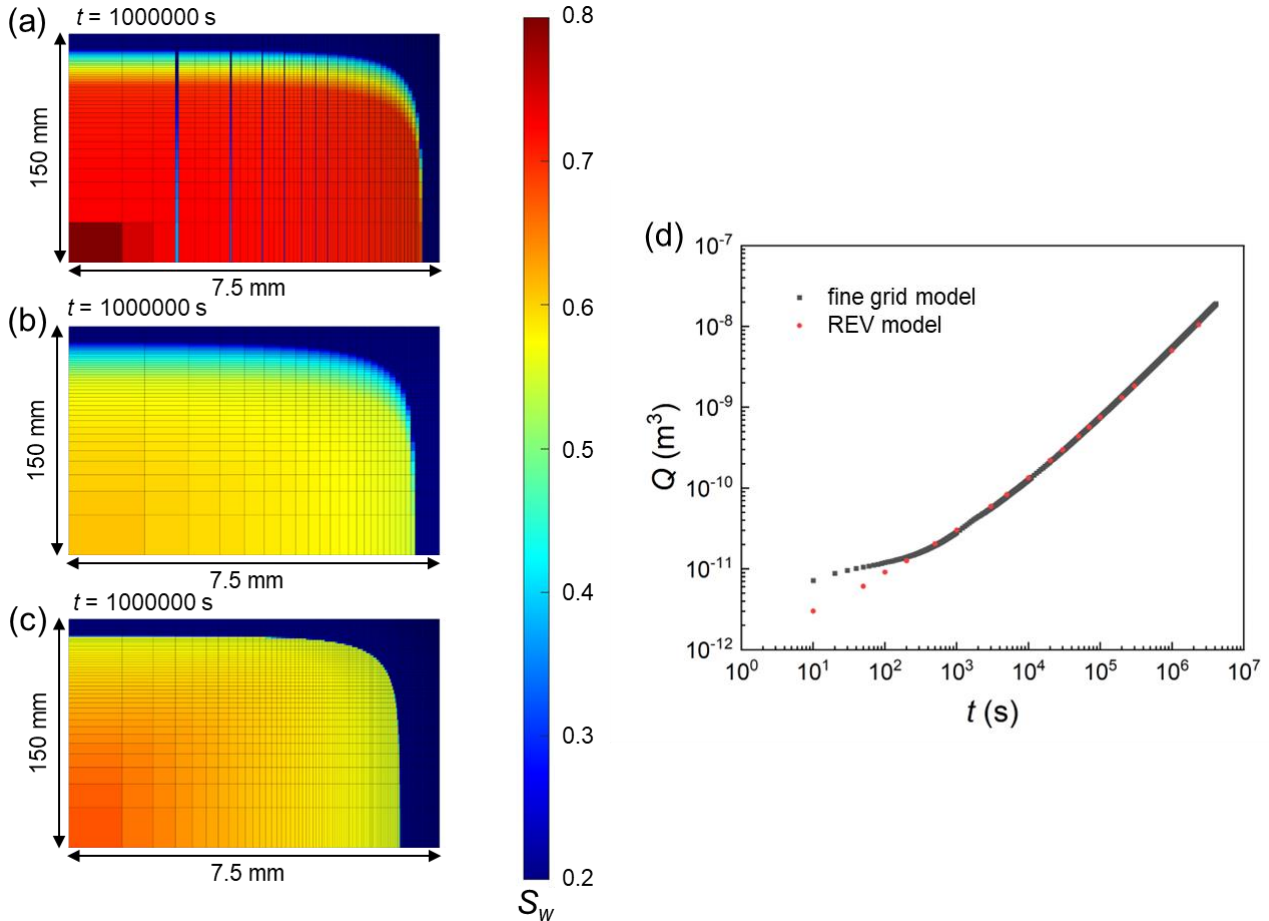
Fig. 18—Water saturation distribution in log-log coordinate and cumulative oil production comparison between fine grid model and equivalent REV model in 2D model at $t = 1000000$ s. (a) Water saturation distribution of fine grid model; (b) Averaged water saturation distribution of fine grid model; (c) Water saturation distribution of equivalent REV model, red represents high water saturation, while blue represents low water saturation; (d) cumulative oil production comparison between fine grid model (black line) and equivalent REV model (red points) at $t = 1000000$ s.

Finite volume method is used to solve the imbibition process of equivalent REV scale model, and the water saturation profile at the same time is shown in **Fig. 18c**. When comparing the averaged water saturation in the fine grid model (**Fig. 18b**), with the water

saturation in the equivalent REV model (**Fig. 18c**), they exhibit a good match. Furthermore, the cumulative oil production evolution obtained from fine grid model simulation and equivalent REV scale model simulation is compared in **Fig. 18d**. The results demonstrate a perfect match at late times (**Fig. 18d**). Grid sensitivity independence is shown in **Fig. S-3**.

In addition, we note that the REV model is not limited to imbibition kinetics. We show that it also works for displacement as shown in the Supplementary Materials and in **Fig. S-13**, when the system fits DPF definition.

VI. Summary and Conclusions

We investigate spontaneous countercurrent imbibition during unconventional hydrocarbon recovery in one common type of unconventional formations, where micro-fractures densely and parallelly develop. The main conclusions are as follows:

- **Definition of DPF system**. A rigorous definition of "dense and parallel micro-fracture" (DPF) system is proposed, as fractured media that the characteristic time of fluid flow along the fracture is much longer than that across the layered matrix. Continental shales are typical DPF systems when spontaneous imbibition occurs, as supported by core characterizations. In a DPF system, classic dual porosity (DP) models are not valid due to the failure of assumptions for fracture-matrix fluid exchange.

- **Spontaneous countercurrent imbibition kinetics in DPF systems**. We conduct fine-grid reservoir simulation to investigate imbibition kinetics in DPF systems. We look into directions both parallel to fracture (x-direction) and perpendicular to the fractures (y-direction). In both directions, early- and late- stages are identified, which are all of diffusive kinetics ($Q \propto t^{1/2}$) but with distinct pre-factors. We focus on late stage for both directions, that are of interest to hydrocarbon. For x-direction imbibition, the larger micro-fracture aperture and spacing as well as the smaller crude oil viscosity contribute to oil production. Matrix permeability has little effect on ultimate recovery. For y-direction imbibition, the smaller micro-fracture aperture, larger matrix permeability and lower crude oil viscosity contribute to higher imbibition rate. Micro-fracture spacing has little effect on ultimate recovery.

- **Theoretical solutions for late stage**. Imbibition kinetics is insensitive to matrix permeability and matrix plays a role of fluid storage space in x-direction; imbibition kinetics is insensitive to fracture permeability, and fracture plays a role of fluid storage space in y-direction. We rationalize these observations based on DPF definition which allows local capillary equilibrium assumption, and then successfully derive analytical solutions for one-dimensional spontaneous countercurrent simulation for both x-direction and y-direction imbibition. Theoretical solutions match fine-grid simulation results.

- **REV scale model and anisotropic relative permeabilities**. According to the theoretical solutions, we construct coarsened REV scale model to depict two-phase flow in DPF systems for reservoir simulation. The model matches two-dimensional fine-grids simulation well. In this REV scale model for DPF systems, we note that the anisotropy cannot be depicted only by anisotropic absolute permeability. Anisotropic relative permeability is necessary, and is rigorously derived. New challenge thus rises for reservoir simulation on unconventional formation with DPF systems, such as continental shale oil.

Although we define DPF systems inspired by direct observation on continental shale, the analytical solution and REV model are not limited to shale systems. Above conclusions should also work for other formations with similar layered properties that satisfy the rigorous definition of DPF.

References

Andersen, P. Ø. 2019. A Simplified Modelling Approach for Petroleum Recovery by Spontaneous Imbibition in Naturally Fractured Reservoirs. *Journal of Natural Gas Science and Engineering* 63: 95–114. https://doi.org/10.1016/j.jngse.2019.01.012.

Andersen, P. Ø., Evje, S., and Kleppe H. 2014. A Model for Spontaneous Imbibition as a Mechanism for Oil Recovery in Fractured Reservoirs. *Transport in Porous Media* 101: 299–331. https://doi.org/10.1007/s11242-013-0246-7.

Barenblatt, G. I., Zheltov, Iu. P., and Kochina, I. N. 1960. BASIC CONCEPTS IN THEORY OF SEEPAGE OF HOMOGENEOUS LIQUIDS IN FISSURED ROCKS [STRATA] 24 (5): 852–864.

Afsharpoor, A., and Javadpour, F. 2016. Liquid slip flow in a network of shale noncircular nanopores. *Fuel* 180 (2016): 580-590.

Brooks, R. H., and Corey, A. T. 1963. HYDRAULIC PROPERTIES OF POROUS MEDIA AND THEIR RELATIONSHIP TO DRAINAGE DESIGN. In *Annual Meeting American Society of Agricultural Engineers*.

Chen, D., Pang, X., and Jiang, F. et al. 2021. Shale Oil Potential and Mobility of Low-Maturity Lacustrine Shales: Implications from NMR Analysis in the Bohai Bay Basin. *Energy and Fuels* 35 (3): 2209–2223. https://doi.org/10.1021/acs.energyfuels.0c03978.

Cui, J. 2019. Oil transport in shale nanopores and micro-fractures: Modeling and analysis. *Journal of Petroleum Science and Engineering* 178(2019): 640-648.

Goda, H. M., and Behrenbruch, P. 2004. Using a Modified Brooks-Corey Model to Study Oil-Water Relative Permeability for Diverse Pore Structures. In *SPE Asia Pacific Oil and Gas Conference and Exhibition*.

Gou, Q., Xu, S., and Hao, F. et al. 2019. Full-Scale Pores and Micro-Fractures Characterization Using FE-SEM, Gas Adsorption, Nano-CT and Micro-CT: A Case Study of the Silurian Longmaxi Formation Shale in the Fuling Area, Sichuan Basin, China. *Fuel* 253: 167–179. https://doi.org/10.1016/j.fuel.2019.04.116.

Gu, Q., Zhu, L., and Zhang, Y. et al. 2019. Pore-Scale Study of Counter-Current Imbibition in Strongly Water-Wet Fractured Porous Media Using Lattice Boltzmann Method. *Physics of Fluids* 31 (8). https://doi.org/10.1063/1.5099500.

Hatiboglu, C. U., and Babadagli, T. 2007. Oil Recovery by Counter-Current Spontaneous Imbibition: Effects of Matrix Shape Factor, Gravity, IFT, Oil Viscosity, Wettability, and Rock Type. *Journal of Petroleum Science and Engineering* 59: 106–122. https://doi.org/10.1016/j.petrol.2007.03.005.

Kazemi, H., Merrill, JR. L. S., and Porterfield, K. L. 1976. Numerical Simulation of Water-Oil Flow in Naturally Fractured Reservoirs. *SPE J.* 16 (06): 317–326.

Keilegavlen, E., Nordbotten, J. M., and Stephansen, A. F. 2012. TENSOR RELATIVE PERMEABILITIES: ORIGINS, MODELING AND NUMERICAL DISCRETIZATION. *International Journal of Numerical Analysis and Modeling* 9.

Kobchenko, M., Panahi, H., and Renard, F. et al. 2011. 4D Imaging of Fracturing in Organic-Rich Shales during Heating. *Journal of Geophysical Research: Solid Earth* 116 (B12). https://doi.org/10.1029/2011JB008565.

Krogstad, S., Lie, K., and Møyner, O. et al. 2015. MRST-AD - an Open-Source Framework for Rapid Prototyping and Evaluation of Reservoir Simulation Problems. In *SPE Reservoir Simulation Symposium*.

Leverett, M. C. 1940. Capillary Behavior in Porous Solids. In *Tusla Meeting*. http://onepetro.org/TRANS/article-pdf/142/01/152/2178004/spe-941152-g.pdf/1.

Li, S., Sang, Q., and Dong, M. et al. 2019. Determination of inorganic and organic permeabilities of shale. *International Journal of Coal Geology* 215. https://doi.org/10.1016/j.coal.2019.103296.

Lukyanov, A. V., Sushchikh, M. M., and Baines, M. J. et al. 2012. Superfast Nonlinear Diffusion: Capillary Transport in Particulate Porous Media. *Physical Review Letters* 109 (21). https://doi.org/10.1103/PhysRevLett.109.214501.

Lukyanov, A. V., Mitkin, V. V., and Theofanous, T. G. et al. 2019. Capillary Transport in Particulate Porous Media at Low Levels of Saturation. *Journal of Applied Physics* 125. https://doi.org/10.1063/1.5086869.

Ma, L., Dowey, P. J., and Rutter, E. et al. 2019. A Novel Upscaling Procedure for Characterising Heterogeneous Shale Porosity from Nanometer-to Millimetre-Scale in 3D. *Energy* 181: 1285–1297. https://doi.org/10.1016/j.energy.2019.06.011.

Mcwhorter, D. B., and Sunada, D. K. 1990. Exact Integral Solutions for Two-Phase Flow. *WATER RESOURCES RESEARCH* 26 (3): 399–413.

Meng, M., Ge, H., and Shen, Y. et al. 2020. The Effect of Clay-Swelling Induced Cracks on Shale Permeability during Liquid Imbibition and Diffusion. *Journal of Natural Gas Science and Engineering* 83. https://doi.org/10.1016/j.jngse.2020.103514.

Meng, Q, Cai, Z., and Cai, J. et al. 2019. Oil Recovery by Spontaneous Imbibition from Partially Water-Covered Matrix Blocks with Different Boundary Conditions. *Journal of Petroleum Science and Engineering* 172: 454–464. https://doi.org/10.1016/j.petrol.2018.09.075.

Meng, Q., Liu, H., and Wang, J. 2016. Effect of Viscosity on Oil Production by Cocurrent and Countercurrent Imbibition from Cores with Two Ends Open. *SPE Reservoir Evaluation and Engineering* 20 (2): 251–259. https://doi.org/10.2118/183635-PA.

Muther, T., Qureshi, H. A., and Syed, F. I. et al. 2022. Unconventional Hydrocarbon Resources: Geological Statistics, Petrophysical Characterization, and Field Development Strategies. *Journal of Petroleum Exploration and Production Technology* 12 (6): 1463–1488. https://doi.org/10.1007/s13202-021-01404-x.

Ougier-Simonin, A., Renard, F., and Boehm, C. et al. 2016. Microfracturing and Microporosity in Shales. *Earth-Science Reviews* 162: 198–226. https://doi.org/10.1016/j.earscirev.2016.09.006.

Panahi, H., Kobchenko, M., and Renard, F. et al. 2013. A 4D Synchrotron X-Ray-Tomography Study of the Formation of Hydrocarbon-Migration Pathways in Heated Organic-Rich Shale. *SPE J.* 18 (02).

Pei, X., Liu, Y., and Gu, W. et al. 2022. Characterization and Analysis of Anisotropic Relative Permeability. *SPE J.* 27 (1): 579–596. https://doi.org/10.2118/206724-PA.

Pei, X., Liu, Y., and Lin, Z. et al. 2023. Anisotropic Characteristics of Relative Permeability in Sedimentary Reservoirs. In *57th US Rock Mechanics/Geomechanics Symposium*.

Polat, C. 2021. Insights into the Solution of Counter-Current Spontaneous Imbibition for Tight Unconventional Reservoirs. *Journal of Petroleum Science and Engineering* 201. https://doi.org/10.1016/j.petrol.2021.108505.

Roy, S., Raju, R., and Chuang, H. F. et al. 2003. Modeling gas flow through microchannels and nanopores. *Journal of Applied Physics* 93 (8): 4870–4879. https://doi.org/10.1063/1.1559936.

Saif, T., Lin, Q., and Butcher, A. R. et al. 2017. Multi-scale multi-dimensional microstructure imaging of oil shale pyrolysis using X-ray micro-tomography, automated ultra-high resolution SEM, MAPS Mineralogy and FIB-SEM. Applied Energy 202(2017): 628:647.

Schmid, K. S., Alyafei, N., and Geiger, S. et al. 2016. Analytical Solutions for Spontaneous Imbibition: Fractional-Flow Theory and Experimental Analysis. *SPE J.* 21 (6): 2308-2316. https://doi.org/10.2118/184393-PA.

Sinn, C. J. A., Klaver, J., and Fink, R. et al. 2017. Using BIB-SEM Imaging for Permeability Prediction in Heterogeneous Shales. *Geofluids* 2017. https://doi.org/10.1155/2017/4709064.

Sirimark, P., Lukyanov, A. V., and Pryer. T. 2018. Surface Permeability of Porous Media Particles and Capillary Transport. *European Physical Journal E* 41 (9). https://doi.org/10.1140/epje/i2018-11716-6.

Sirimark, P., Lukyanov, A. V., and Pryer. T. 2019. Surface Permeability of Particulate Porous Media. *Transport in Porous Media* 130: 637–654. https://doi.org/10.1007/s11242-019-01332-9.

Sun, L., He, W., and Feng, Z. et al. 2022. Shale Oil and Gas Generation Process and Pore Fracture System Evolution Mechanisms of the Continental Gulong Shale, Songliao Basin, China. *Energy and Fuels* 36 (13): 6893–6905. https://doi.org/10.1021/acs.energyfuels.2c01407.

Tian, W., Wu, K., and Gao, Y. et al. 2021. A Critical Review of Enhanced Oil Recovery by Imbibition: Theory and Practice. *Energy and Fuels* 35 (7): 5643–5670. https://doi.org/10.1021/acs.energyfuels.1c00199.

Velasco-Lozano, M., and Balhoff. M. T. 2021. A Semi-Analytical Solution for Countercurrent Spontaneous Imbibition in Water-Wet Fractured Reservoirs. *Transport in Porous Media* 138 (1): 77–97. https://doi.org/10.1007/s11242-021-01591-5.

Wang, J., Xie, H., and Li, C. 2021. Anisotropic Failure Behaviour and Breakdown Pressure Interpretation of Hydraulic Fracturing Experiments on Shale. *International Journal of Rock Mechanics and Mining Sciences* 142. https://doi.org/10.1016/j.ijrmms.2021.104748.

Wang, Q., Lyu, C., and Cole, D. R. 2019. Effects of Hydration on Fractures and Shale Permeability under Different Confining Pressures: An Experimental Study. *Journal of Petroleum Science and Engineering* 176: 745–753. https://doi.org/10.1016/j.petrol.2019.01.068.

Wang, X., Chen, J., and Ren, D. et al. 2020. Role of Gas Viscosity for Shale Gas Percolation. *Geofluids* 2020. https://doi.org/10.1155/2020/8892461.

Warren, J. E., and Root, P. J. 1963. The Behavior of Naturally Fractured Reservoirs. *SPE J.* 3 (03): 245–255.

Xu, Y., Lun, Z., and Pan, Z. et al. 2022. Occurrence Space and State of Shale Oil: A Review. *Journal of Petroleum Science and Engineering* 211. https://doi.org/10.1016/j.petrol.2022.110183.

Xue, L., Guo, X., and Chen, H. 2020. *Fluid Flow in Porous Media*. Singapore: World Scientific.

Zhang, Y., Zhang, J., and Yuan, B. et al. 2018. In-Situ Stresses Controlling Hydraulic Fracture Propagation and Fracture Breakdown Pressure. *Journal of Petroleum Science and Engineering* 164: 164–173. https://doi.org/10.1016/j.petrol.2018.01.050.

Zhang, T., Li, X., and Yin, Y. et al. 2019. The transport behaviors of oil in nanopores and nanoporous media of shale. *Fuel* 242: 305-315. https://doi.org/10.1016/j.fuel.2019.01.042.

Zhu, W., Pan, B., and Chen, Z. et al. 2023. Transport in Nanoporous Media. *Engineering*. https://doi.org/10.1016/j.eng.2023.05.014.

Zou, C., Yang, Z., and Cui, J. et al. 2013. Formation Mechanism, Geological Characteristics and Development Strategy of Nonmarine Shale Oil in China. *Petroleum Exploration and Development* 40 (1): 15–27. https://doi.org/10.1016/S1876-3804(13)60002-6.